The VST ATLAS Quasar Survey: Catalogue and Weak Gravitational Lensing Analyses

ALICE MARILYN ELTVEDT

The VST ATLAS Quasar Survey: Catalogue and Weak Gravitational Lensing Analyses

Alice Eltvedt

Abstract: We develop selection criteria for a $g < 22.5$ quasar catalogue based on VST ATLAS+unWISE and aimed at competing with DESI to reach a quasar sky density of 130 deg^{-2}. Ultimately this catalogue can be used to help select quasar targets for the eROSITA AGN + 4MOST Cosmology Redshift Surveys. To guide our selection, we use deep X-ray/optical/NIR/MIR data in the extended William Herschel Deep Field (WHDF) as well as the selections performed on DECaLS and NEOWISE data by DESI Collaboration et al. (2016). Accordingly adjusting our ATLAS+unWISE criteria and applying over the ~ 4000 deg^2 ATLAS survey gives us a total number of quasar candidates to $g < 22.5$ of ~ 704000 i.e. a sky density of 170 deg^{-2} of which $\sim 85\%$ or 600000 are likely to be $0.7 < z < 2.3$ quasars as confirmed by comparisons with 2QZ, eBOSS and 2QDESp spectroscopic surveys. We find that the QSO sky density at $g < 22.5$ may be as high as 204 deg^{-2} with the inclusion of quasars morphologically mis-classified as galaxies that otherwise satisfy the usual $ugri$ and $giW1$ selections. We assume an efficiency of 60% for these quasar candidates, therefore giving us a final quasar sky density of ~ 120deg^{-2}. We then cross-correlate a low-contamination subset of this QSO catalogue with $g < 20.5$ galaxy clusters and $r < 21$ galaxies to detect quasar magnification bias caused by weak lensing. From this analysis we confirm previous results of Myers et al. (2003) and Scranton et al. (2005). We also detect lensing of the Cosmic Microwave Background by our quasar sample, finding remarkable agreement between our result and the ones achieved by Geach et al. (2019) and Chehade et al. (2016).

The VST ATLAS Quasar Survey: Catalogue and Weak Gravitational Lensing Analyses

Alice Eltvedt

A Thesis presented for the degree of
Master of Science by Research

Centre for Extragalactic Astronomy
Department of Physics
Durham University
United Kingdom

January 2020

Contents

List of Figures

List of Tables

Declaration

The work in this thesis is based on research carried out in the Centre for Extragalactic Astronomy, Department of Physics, Durham University, United Kingdom. No part of this thesis has been submitted elsewhere for any other degree or qualification and it is all my own work unless referenced to the contrary in the text.

Acknowledgements

I would like to thank my advisors, Prof. Tom Shanks and Dr. Nigel Metcalfe, for all of their insight, guidance, patience, and support over this past year. Without their knowledge and encouragement this thesis would not have been possible.

Many thanks also to Prof. Tom Shanks for providing unending help tackling not only my academic work, but ensuring a smooth transition to a new school and country. Additional thanks goes to Behzad Ansarinejad for his constant advice, discussions, and willingness to help. Thank you to my office mates, Giorgio Manzoni, Jack Birkin, and Miguel Icaza, for being wonderfully compassionate and supportive throughout this whole process. Thank you to Prof. David Alexander for welcoming me to wider research groups and creating a supportive community within the department.

I also thank Durham University Sport, especially my fellow water polo players, for listening to all my concerns, providing endless encouragement, and being a wonderful source of fun and stress relief.

Finally, without my family I would never have been able to do any of the work that I have accomplished. Thank you to my parents, Simone and Anthony, for always believing in me and supporting my goals. Thank you to my siblings, Louise, Mickey, Maya, and Layla, for being rays of sunshine in my life.

Chapter 1

Introduction

The detection of the accelerated expansion of the universe (e.g. Riess et al. (1998), Perlmutter et al. (1999)) as well as the existence of dark matter (Zwicky (1933), Rubin et al. (1977)), as necessitated by the currently accepted ΛCDM model of the universe, has made the undisputed determination and understanding of these phenomena a main goal of modern astrophysics. The existence of dark energy is one possibility to explain the accelerated expansion of our universe within the framework of Einstein's theory of general relativity (e.g. Ratra & Peebles (1988)) and dark matter is needed to explain observations of the clustering of structures (e.g. Peebles (1980)). Therefore, we must investigate methods to measure the accelerated expansion of the universe, such as measurements of Baryon Acoustic Oscillations (BAO) (Eisenstein et al. (2005)), as well as conducting gravitational lensing analyses which can be used to measure the observed mass in the universe in order to confirm the need for dark matter (e.g. Kaiser & Squires (1993), Kaiser (1998), Myers et al. (2003)).

The accelerated expansion of the universe was first observed through the Hubble diagram of Type Ia Supernova (e.g. Riess et al. (1998), Perlmutter et al. (1997)). This was then confirmed by measuring the clustering of galaxies, quasars, and hydrogen clouds. Detections of BAO are used here as a standard rod, or ruler, to measure scale length and draw the Hubble diagram. BAOs originate from the propagation of waves in primordial density fluctuations (e.g. Peebles & Yu (1970), Peebles (1980)). Within overdense regions, gravitational attraction of baryonic matter and outward radiation pressure of photons leads to the BAO seen as a wave which expands in spherical shells from these overdense regions. This acoustic wave can be detected at a scale of $\approx 150\ h^{-1}$Mpc. The invariance of the BAO scale allows it to be used as a standard ruler to confirm distance measurements of large scale structure. The

CMB acoustic peaks and corresponding BAO features probe the cosmological model (e.g. Sakharov (1966)). Our ultimate aim here is to use quasars as tracers of the mass distribution and hence as probes of the BAO scale.

In this thesis we develop selection criteria for a photometrically selected quasar catalogue based on VST ATLAS+unWISE (Shanks et al. (2015), Schlafly et al. (2019)). The catalogue is aimed at ~ 0.5 million $0.7 < z < 2.3$ quasar candidates at $g < 22.5$. We aim to achieve a sky density of 130 deg^{-2} over ~ 4000 deg^2, comparable to the sky densities projected by DESI Collaboration et al. (2016). This catalogue aims to prepare the spectroscopic fiber targeting of the upcoming eROSITA AGN and 4MOST Cosmology Redshift Surveys (Merloni et al. (2012), Richard et al. (2019)). The production of this quasar catalogue will form the major objective of this thesis.

The long-term aims of this quasar survey are to probe the nature of dark energy and dark matter via BAO and redshift space distortion analyses (e.g. Kaiser (1987)) of the final 4MOST redshift surveys. The dark energy equation of state will be measured through its effect on the Universal expansion rate. We shall also perform tests of modified gravity models as an alternative explanation of the accelerating Universe via quasar z-space distortions in the future.

In this thesis we shall report first on preliminary weak gravitational lensing analyses through the lensing of our quasar candidates by foreground galaxies and galaxy clusters. Through this cross-correlation we will be able to fit halo models to our data in order to calculate galaxy cluster halo masses and dispersion velocities (e.g. Mo & White (1996)). We shall also detect the deflection (lensing) of the Cosmic Microwave Background (CMB) (Planck Collaboration et al. (2018)) by our quasar candidates through a cross-correlation of our QSO survey and the Planck CMB lensing map (e.g. Geach et al. (2019), Han et al. (2019)). This allows us to directly measure the quasar bias and quasar host halo masses.

Chapter 2

Data

In this chapter we will describe the data catalogues used in the analyses performed in this thesis. These are utilized in the creation of our VST-ATLAS quasar catalogue as well as the resulting weak gravitational lensing analyses.

2.1 VST ATLAS

The ESO VST ATLAS data we utilize in this work is from the newly available DR4 ESO catalogue. ATLAS is a photometric survey which images ~ 4000 deg^2 of the Southern sky (~ 1300deg^2 in the NGC and ~ 2700deg^2 in the SGC) in the $ugriz$ bands, designed to probe similar depths as SDSS. The imaging is performed with the VLT Survey Telescope (VST), which is a 2.6-m wide-field survey telescope with a $1^\circ \times 1^\circ$ field of view. It is equipped with the OmegaCAM camera (Kuijken et al. (2002)), which is an arrangement of 32 CCDs with $2k \times 4k$ pixels, resulting in a $16k \times 16k$ image with a pixel scale of $0.''21$. The two sub-exposures taken per 1 degree field are processed and stacked by the Cambridge Astronomy Survey Unit (CASU). This pipeline provides catalogues with approximately 5σ source detection that include fixed aperture fluxes and morphological classifications. The processing pipeline and resulting data products are described in detail by Shanks et al. (2015). We create bandmerged catalogues using TOPCAT. For our quasar catalogue, we utilize a $1.2''$ radius aperture (aper3 in the CASU nomenclature), and the morphological star-galaxy classification supplied as a default in the CASU catalogues. This classification is discussed in detail by González-Solares et al. (2008). We also try to improve this classification using other algorithms, including ANNz2 (see Chapter 4), also used for estimating photo-z for the quasars.

2.2 unWISE

The unWISE catalogue (Schlafly et al. (2019)) presents ∼two billion objects observed by WISE, with deeper imaging and improved modelling over AllWISE. The NASA satellite Wide-field Infrared Survey Explorer (WISE) (Wright et al. (2010)), mapped the entire sky in four pass-bands $W1$, $W2$, $W3$, and $W4$ at 3.4, 4.6, 12, and 22μm respectively, with 5σ point source limits at $W1 = 16.83$ and $W2 = 15.60$ mag in the Vega system. However, the unWISE catalogue detects sources approximately 0.7 magnitudes fainter than AllWISE in $W1$ and $W2$, ie 5σ limits of $W1 = 17.5$ and $W2 = 16.3$ in the Vega system. This deeper imaging is made possible through the coaddition of all available $3 - 5\mu m$ WISE imaging, including that from the ongoing NEOWISE-Reactivation mission, increasing the total exposure time by a factor of ~ 5 relative to AllWISE (Schlafly et al. (2019)).

2.3 2QZ

The 2dF QSO Redshift Survey (2QZ; Boyle et al. (2002), Croom et al. (2005)) covers approximately 750 deg^2 of the sky, using the 2-degree Field (2dF) multi-object spectrograph at the Anglo Australian Telescope (AAT) to target sources, and discovered $\sim$ 23000 quasars at $z < 3$. The areas targeted for 2QZ are contained within the 2dF Galaxy Redshift Survey sky coverage (Colless et al. (2001), 2dFGRS). The $\sim$ 375 deg^2 SGC subset of 2QZ overlaps the ATLAS SGC area. The 2QZ catalogue utilizes photometric colour cuts to select quasar targets. Therefore, we can use the 2QZ quasar catalogue to test for completeness of our catalogue and train our photo-z algorithm as the catalogue spans a redshift range of $0.3 < z < 2.2$, which includes our target redshift range. At higher redshifts, the UVX technique fails as the Lyman-alpha forest enters the u-band, and the completeness of the 2QZ survey rapidly drops. Additional incompleteness may be due to AGN dust absorption. See Croom et al. (2005) for further description of 2QZ QSO survey.

2.4 2SLAQ

The 2SLAQ redshift survey (da Ângela et al. (2008)) partly overlaps with subregions of the 2QZ NGC area, with spectroscopically confirmed quasars at redshifts of $0 < z < 3$. These

quasars are selected based on SDSS photometry, which is similar to the selection method we employ. The redshifts were measured for quasars of apparent magnitudes $20.5 < g_{SDSS} < 21.85$.

2.5 2QDESp

The 2QDES Pilot Survey (2QDESp) (Chehade et al. (2016)) was the first survey to use VST ATLAS photometry to target quasars. They attempted to target quasars up to $g < 22.5$, with high completeness up to $g = 20.5$ with an average quasar sky density of 70 deg^{-2} in the redshift range of $0.8 < z < 2.5$. The target depth of $g \leq 22.5$ was to probe the properties of these faint quasars as this is a relatively unexplored depth for the targeted redshift range. Note that the SDSS Stripe 82 Survey of (Palanque-Delabrouille et al. (2011)) covered ≈ 15 deg^2 to such faint magnitudes, however in a smaller redshift range of $1 \leq z \leq 2.2$.

We base our selection methods on the 2QDESp selection criteria as we aim to find sources at these faint magnitudes with a higher sky density. We are able to select fainter targets as we use the unWISE catalogue in conjunction with VST ATLAS photometry, instead of the WISE all-sky source catalogue. We are also able to take advantage of the full VST ATLAS catalogue as it was not completed at the time of 2QDESp.

2.6 WHDF

To perform an analysis of X-ray selected quasars, we use the William Herschel Deep Field (WHDF) data provided by Metcalfe et al. (2001). This data covers a 16×16 arcminute^2 patch of sky with data in the UBRIZHK bands. We convert the UBRIZHK band data to $ugri$ to perform an accurate comparison between the WHDF and ATLAS data. This is then combined with Chandra X-ray data as well as the MIR 3.6 and 4.5μm Spitzer SpIES data to get $W1$ and $W2$ band information (Timlin et al. (2016)).

2.7 DECaLS + NEOWISE

To allow checks of unWISE quasar selection, we download a sweep from the DECaLS Legacy Archive DR7 as this is the data which has been used by DESI Collaboration et al. (2016) in

their science, targeting, and survey design. This DR7 is a public data release which includes catalogues from the DECam Legacy Survey. This also includes the $W1$, $W2$, $W3$, and $W4$ WISE fluxes using forced photometry at the locations of Legacy Surveys optical sources in the unWISE maps.

Chapter 3

VST ATLAS QSO Selection

3.1 Introduction

To create the VST ATLAS quasar catalogue, we use photometric selection methods in multiple colour spaces based on previous work done on VST ATLAS+unWISE and WHDF data. We also compare with the proposed selection for DESI.

We utilize both the UVX and the Infrared excess properties of quasars to create photometric colour cuts for our target selection, initially following Chehade et al. (2016). We adjust our initial selections due to the increased depth of our catalogue to further decrease stellar contamination while maximizing completeness of the quasar target sample. We perform these colour cuts in the regions covered by VST-ATLAS and unWISE in both the Northern and Southern Galactic Caps in the Southern hemisphere. The colour cuts made to distinguish quasar candidates through the UVX property were also used by 2QZ and SDSS to select quasars in our target redshift range of $0.8 < z < 2.4$. As the VST-ATLAS *ugriz* photometric bands are similar to SDSS and 2QZ, we can test our photometric selections on overlapping areas.

3.2 2QDESp QSO Selection

Our initial ATLAS selections are based on the UVX and mid-IRX quasar selections made by Chehade et al. (2016) for the 2QDES pilot survey, with the deeper unWISE replacing

AllWISE as the MIR survey. The UVX selections are made in the $u-g$ vs. $g-r$ and $g-r$ vs. $r-i$ colour spaces. The mid-IRX selections are made in the $g-i$ vs. $i-W1$ and g vs. $W1-W2$ colour spaces. Chehade et al. (2016) utilize a combination of VST-ATLAS and WISE photometry in ~ 150 deg^2 of the Southern hemisphere for their analysis. We expand and improve this selection by using VST-ATLAS and unWISE photometry over ~ 4000 deg^2 of the Southern hemisphere.

The original colour selections from Chehade et al. (2016) are as follows. The VST ATLAS photometry is in AB magnitudes and the unWISE photometry is in Vega magnitudes. The UVX/optical selection is:

- $-1 \leq (u-g) \leq 0.8$
- $-1.25 \leq (g-r) \leq 1.25$
- $(r-i) \geq 0.38 - (g-r)$

The selections targeting mid-IR excess are:

- $(i-W1) \geq (g-i) + 1.5$
- $-1 \leq (g-i) \leq 1.3$
- $(i-W1) \leq 8$
- $(W1-\mathrm{W2}) > 0.4$ for $g < 19.5$
- $(W1-\mathrm{W2}) > -0.4g + 8.2$ for $g > 19.5$

For reference, these selections can be seen in Figure. 3.1, which was taken from Chehade et al. (2016), Figure 1. The $W1-W2$ selection was effectively switched off at $g > 19.5$ due to the increased noise from stars. We expect this noise to be less in our data as we probe deeper in the $g-$, $W1-$, and $W2-$ bands than Chehade et al. (2016). Following the colour selections outlined above, we get an average quasar candidate sky density of 107 deg^{-2}, up from the maximum quasar candidate sky density of 90 deg^{-2} achieved by Chehade et al. (2016). However, this leaves us below our target density of 130 deg^{-2} and motivates us to further improve this selection.

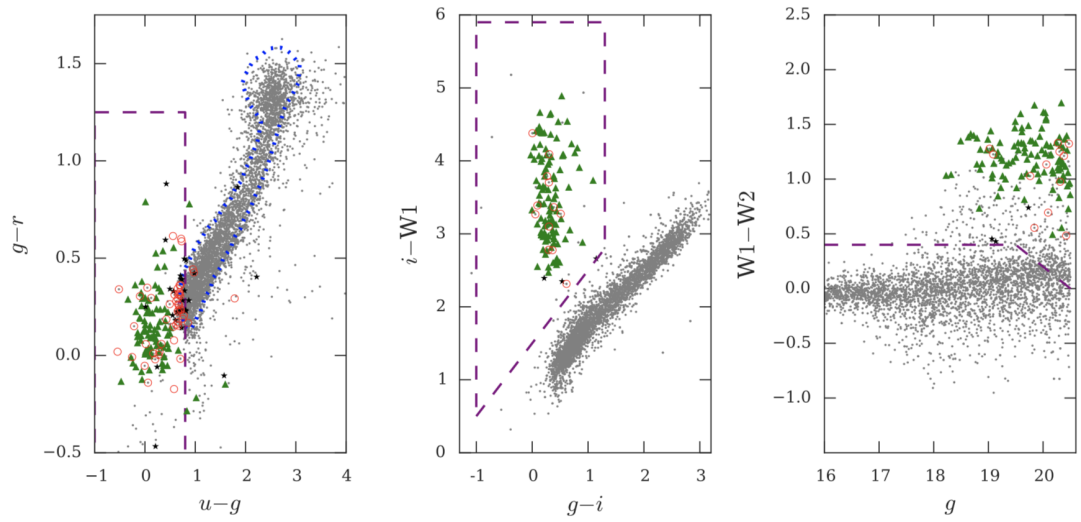

Figure 3.1: This figure, taken from Chehade et al. (2016) shows the ugr, $giW1$, and $gW1W2$ colour spaces. The grey dots are all objects identified in the g-band as point-sources (between $16 \leq g \leq 20.5$). They show the SDSS Stripe 82 stellar locus as a blue dotted line and the ugr colour cuts as purple dashed lines. Spectroscopically confirmed quasars within our target redshift range (0.8<z<2.4) are shown as green triangles and confirmed stars are shown as black five-point stars. Sources without a positive identification are outlined with a red circle.

3.3 William Herschel Deep Field (WHDF) Selection

To further inform our colour cuts for quasar selection, we look at objects in the extended William Herschel Deep Field (Metcalfe et al. (2001), Metcalfe et al. (2006)). Here we have high signal-to-noise optical data which is several magnitudes fainter than the VST-ATLAS data, where we can look to maximize completeness in our selection methods. To do this, we use the R-selected aperture colour image lists provided on the WHDF webpage (http://astro.dur.ac.uk/ nm/pubhtml/herschel/herschel.php) and then match this catalogue to the MIR 3.6 and 4.5μm Spitzer SpIES data (Timlin et al. (2016)) in the WHDF field to get $W1$ and $W2$ band photometry. We convert these UBRIZ Johnson magnitudes to SDSS $ugri$ photometry using the following colour equations for each band in the catalogue (received from Nigel Metcalfe, private communication):

- $g_{sdss} = B - (0.19 * (B - R) + 0.18)$
- $r_{sdss} = R - (-0.2 * (R - I) - 0.04 * (R - I)^3 - 0.1)$
- $i_{sdss} = I - (-0.34 * (R - I) - 0.26)$
- $z_{sdss} = Z - (-0.04 * (R - I) - 0.5)$
- $u_{sdss} = U + 0.8$

X-ray Number Counts in WHDF for redshift and magnitude ranges			
Selections	total number	stars	galaxies
total ($0.3 < z < 3$)	15	10	5
$0.7 < z < 2.3$	11	6	5
$0.3 < z < 3$ & $g < 22.5$	13	10	3
$0.7 < z < 2.3$ & $g < 22.5$	9	6	3

Table 3.1: Number counts for the morphological classifications of the X-ray quasars from Bielby et al. (2012).

- $(i_{sdss} - W1) = 1.35 * (I - W1) - 0.05$

We convert from WHDF UBRIZ to these magnitudes as the VST-ATLAS data has *ugriz* photometry, close to SDSS. Therefore, we are able to utilize selection methods using WHDF as well as previous works such as Chehade et al. (2016).

3.3.1 WHDF X-ray Quasar Population

We can determine preliminary WHDF quasar populations by looking at Table 2 of Bielby et al. (2012), which lists 15 spectroscopically confirmed quasars, their X-ray fluxes, and redshifts in the WHDF. We match these objects to our WHDF photometric data by RA and DEC in order to have their $ugrizW1W2$ magnitudes and morphological classification. These objects are described in Table. 3.1. We see that to a depth of $g < 22.5$ we detect 13 of the Chandra X-ray sources. Of these 13 quasars, 10 are morphologically classified as stellar sources in the WHDF photometric catalogue, and 3 are classified as galactic sources. Additionally, 9 of these 13 quasars are in our target redshift range of $0.7 < z < 2.3$. Therefore, based on this Chandra X-ray data, 13 sources in the WHDF would give us a sky density of 183 ± 49 deg^{-2}. In our target redshift range, the 9 Chandra sources give a sky density of 127 ± 42 deg^{-2}. This is in good agreement with our expected quasar density of 130 deg^{-2} at $g < 22.5$ and $0.7 < z < 2.3$. The full $ugrizW1W2$ information of these 15 objects as well as the original IDs and spectroscopic redsifts, as found by Bielby et al. (2012), are shown in Table 3.2.

Based on these estimates, we aim to find a minimum of $\sim 127 \pm 42$ candidates deg^{-2} with our photometric selection methods. We also use these 15 X-ray selected objects to determine if X-ray selections, e.g. from eROSITA, can further inform our photometric cuts to have a more complete sample of quasar candidates.

WHDF X-Ray Quasars Bielby									
ID	morphology	u	g	r	i	z	W1	W2	z
WHDFCH005	star	21.44	20.52	20.61	20.44	20.43	16.56	15.51	0.52
WHDFCH007	galaxy	23.82	23.25	22.94	22.30	21.29	16.07	15.07	1.33
WHDFCH008	galaxy	24.76	22.03	20.35	19.71	19.32	15.78	15.49	2.12
WHDFCH016	star	21.7	21.01	20.98	20.7	20.64	17.29	16.07	1.73
WHDFCH017	star	20.45	19.56	19.55	19.25	18.84	15.21	14.46	0.40
WHDFCH020	galaxy	22.44	21.89	21.68	21.23	20.89	16.59	16.08	0.95
WHDFCH036	star	23.11	21.2	21.19	20.96	20.64	16.27	15.48	0.83
WHDFCH044	star	23.1	21.8	20.50	19.72	19.09	13.63	12.47	0.79
WHDFCH048	galaxy	23.24	22.95	22.38	22.19	21.93	16.39	15.35	1.52
WHDFCH055	star	23.37	22.21	21.72	21.08	20.77	16.34	15.89	0.74
WHDFCH090	star	21.24	20.36	20.17	20.14	20.23	16.35	15.39	1.32
WHDFCH099	star	20.77	20.45	20.35	20.18	20.07	15.67	14.89	0.82
WHDFCH109	star	18.79	18.24	18.29	18.21	18.35	13.89	12.88	0.57
WHDFCH110	galaxy	22.82	22.02	21.29	20.52	20.08	15.58	15.35	0.82
WHDFCH113	star	22.06	21.09	21.06	21.16	21.11	18.39	17.39	2.55

Table 3.2: Full colour, morphology, and redshift information for the 15 X-ray quasars from Bielby et al. (2012). Obscured quasars are bolded.

3.3.2 WHDF Selection Based Quasar Cuts

To test our selection methods, we perform initial $ugri + giW1W2$ photometric cuts, as derived from previous work done by Chehade et al. (2016), on the 15 confirmed quasars from Chehade et al. (2016) and the WHDF photometric catalogue. As the WHDF photometry is much deeper and less noisy, with $R = 25.5$ at 3σ, we adjust these colour cuts to reflect the decrease in contamination in this area. We also account for slight residual offsets still present in the u- and g-bands. These are probably due to uncertenties in the colour transforms used. We compare Fig. 3.1 to Fig. 3.2 and see that in the WHDF data, the stellar locus and quasars are closer together and have shifted redder than we would have expected from the VST-ATLAS data. Our colour selections reflect the changes we make to increase completeness and decrease contamination in the selections.

Stellar Cuts

We first perform the selections on objects that are morphologically classified in the WHDF data as stellar sources. The $ugri$ selections we are making for stellar candidates are:

- $-0.5 \leq (u - g) \leq 1.0$
- $-0.4 \leq (g - r) \leq 1.35$

- $(r - i) \geq -0.1 - (g - r)$

Additionally we create the following cuts to increase completeness along the stellar locus (see Fig. 3.2) while avoiding features in the stellar horizontal branch (HB):

- $(u - g) > 1.0$ & $(g - r) < -0.9 * (u - g) + 0.8$
- $(u - g) > 1.0$ & $(g - r) > 0.5 * (u - g)$

Our mid-IR, $giW1W2$ selections are:

- $(i - W1) \geq (g - i) + 1.5$
- $-1 \leq (g - i) \leq 2.35$
- $(i - W1) \leq 8$
- $(W1 - W2) > 0.4$

These selections can be seen in Fig. 3.2, Fig. 3.3, Fig. 3.4, and Fig. 3.5. In these figures, objects which are classified as stellar sources are shown in light gray. The stellar locus can be clearly seen in all three colour spaces. In Fig. 3.2 we see that in the UVX region ($u - g < 1$) there is some tendency for the Bielby X-ray sources that have a morphological classification as a star to have slightly bluer $g-r$ colors than the objects with a morphological classification as a galaxy. In Fig. 3.3 the diagonal cut was used by Chehade et al. (2016) to remove stellar white dwarfs (WD). This cut is also similar to the $g - i > -1.0$ cut in Fig. 3.4, which shows excellent separation of main sequence stars and quasars. However, we will see that the galaxy population overlaps the quasar locus. In Fig. 3.5 the two sources that are not selected are are morphologically classified as galaxies.

Extended Source Cuts

As 5 of the 15 confirmed quasars from Bielby et al. (2012) are morphologically classified as extended sources (galaxies) in the WHDF catalogue, we perform our colour selections on extended sources as well. Down to our $g-$band limit of $g < 22.5$, the star/galaxy separation in the WHDF data isn't entirely reliable, so our decision to include this selection is further

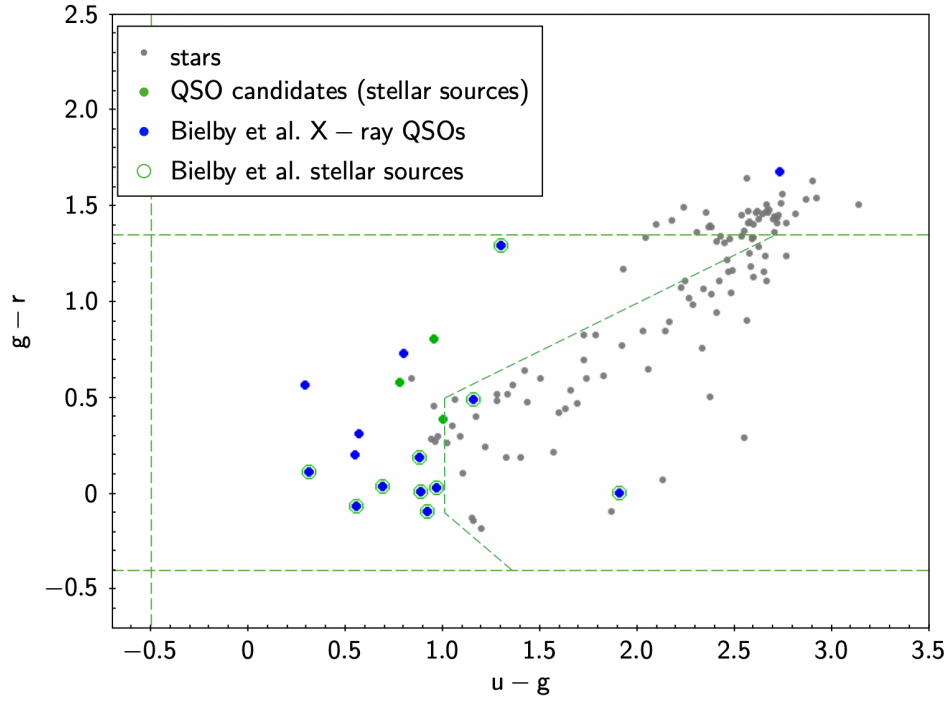

Figure 3.2: Colour selections performed on stellar sources in the extended WHDF in the ugr colour space. Stars are shown in gray. X-ray quasars from Bielby et al. (2012) are shown in blue. The objects selected with our $ugr + giW1$ colour selections on objects classified as stars are shown in green. The confirmed X-ray quasars that are classified as stellar sources are outlined in green and our cuts are shown as green dashed lines.

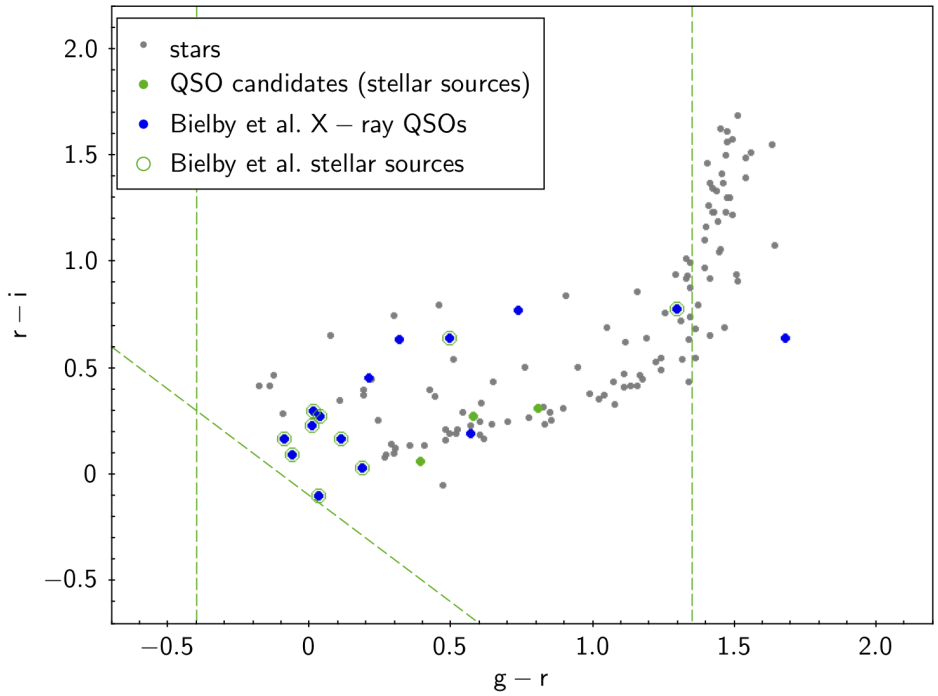

Figure 3.3: Colour selections performed on stellar sources in the extended WHDF in the *gri* colour space. Stars are shown in gray. X-ray quasars from Bielby et al. (2012) are shown in blue. The objects selected with our $ugr + giW1$ colour selections on objects classified as stars are shown in green. The confirmed X-ray quasars that are classified as stellar sources are outlined in green and our cuts are shown as green dashed lines.

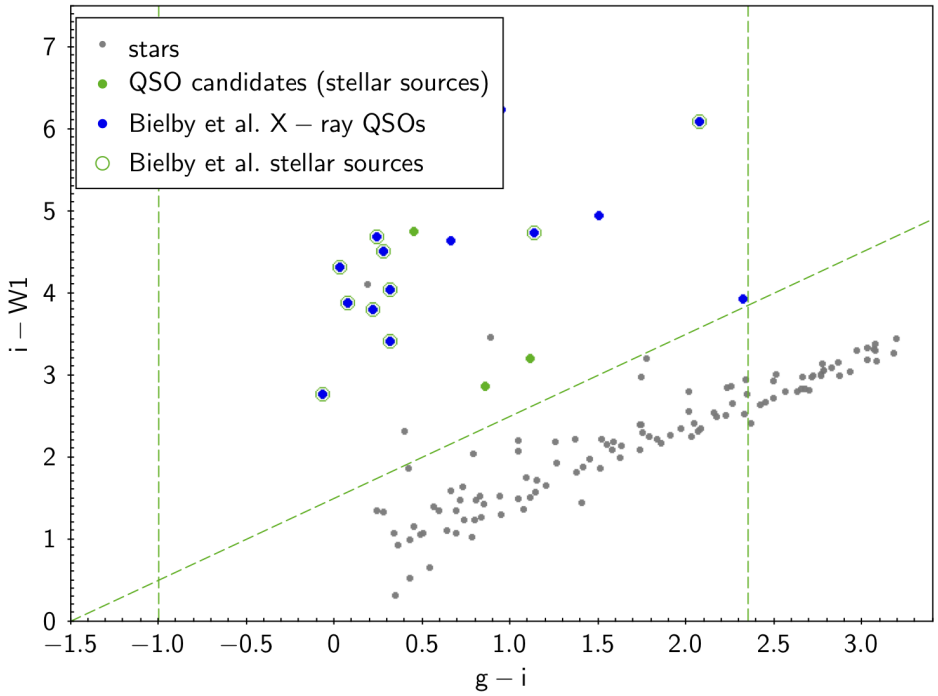

Figure 3.4: Colour selections performed on stellar sources in the extended WHDF in the $giW1$ colour space. Stars are shown in gray. X-ray quasars from Bielby et al. (2012) are shown in blue. The objects selected with our $ugr + giW1$ colour selections on objects classified as stars are shown in green. The confirmed X-ray quasars that are classified as stellar sources are outlined in green and our cuts are shown as green dashed lines.

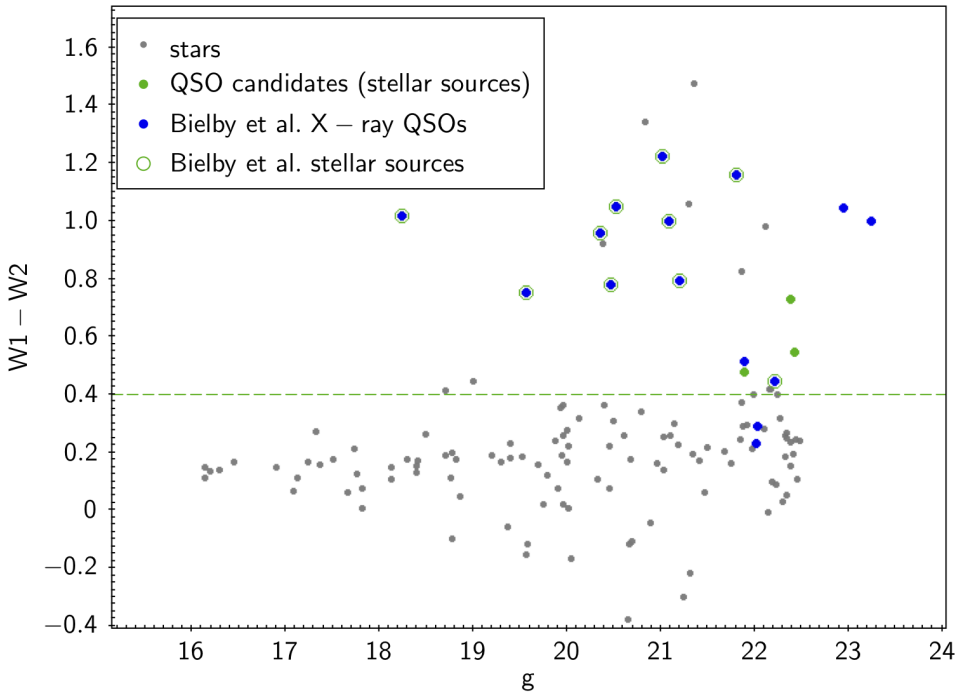

Figure 3.5: Colour selections performed on stellar sources in the extended WHDF in the $gW1W2$ colour space. Stars are shown in gray. X-ray quasars from Bielby et al. (2012) are shown in blue. The objects selected with our $ugr + giW1$ colour selections on objects classified as stars are shown in green. The confirmed X-ray quasars that are classified as stellar sources are outlined in green and our cuts are shown as green dashed lines.

justified when looking at fainter objects.

These selections are shown in Fig. 3.6, Fig. 3.7, Fig. 3.8, and Fig. 3.9. To reduce contamination from galaxies, we modify the $u - g$ v. $g - r$ and the $g - i$ v. $i - W1$ colour spaces. We are then able to cut down possible contamination from galaxies in both colour spaces while retaining possible quasars that have been mis-classified as galaxies. We also restrict the $W1-W2$ cut to $g < 21.9$ to maximize completeness of the selection at fainter magnitudes.

These restricted $ugri$ cuts for extended sources are as follows:

- $-0.5 \leq (u - g) \leq 0.65$
- $-0.4 \leq (g - r) \leq 0.4$
- $(r - i) \geq -0.1 - (g - r)$

The restricted mid-IR, $giW1$ cuts are:

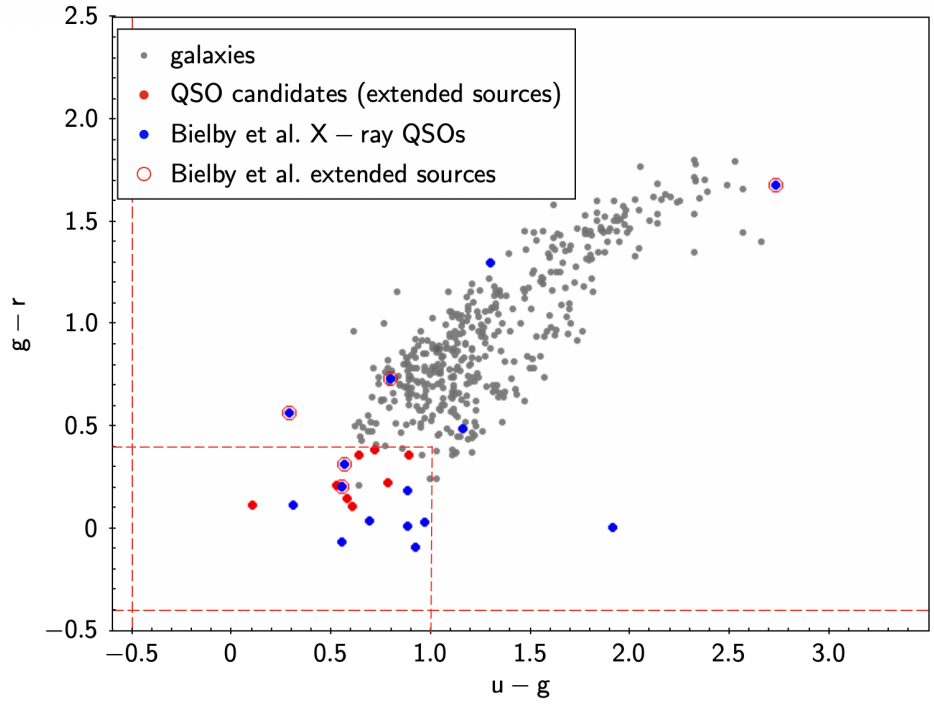

Figure 3.6: Colour selections performed on extended sources in the WHDF in the *ugr* colour space. Extended sources (galaxies) are shown in gray. X-ray QSOs from Bielby et al. (2012) are shown in blue. The objects selected with our $ugr + giW1$ colour selections on objects classified as galaxies are shown in red. Our restricted cuts for galaxies are shown as red dashed lines.

- $(i - W1) \geq (g - i) + 2.7$
- $-1 \leq (g - i) \leq 2.35$
- $(i - W1) \leq 8$
- $(W1 - W2) > 0.4$ & $g < 21.9$

We check the resulting quasar candidates to see if they have recorded Chandra fluxes to help reduce contamination. From this analysis, we find that 5 of the 9 candidates selected as galaxies are faint, hard X-ray sources, which make them more likely to be possible quasars. An additional object is a soft x-ray source. Visual inspection showed 4/5 hard X-ray source galaxies as possible point sources. This is encouraging for the addition of this selection.

Joint Stellar+Extended Sources

We perform both stellar and extended $ugri + giW1$ selections on the 15 X-ray quasars. The number counts for the stellar selection can be seen in Table 3.3. Here we can see the com-

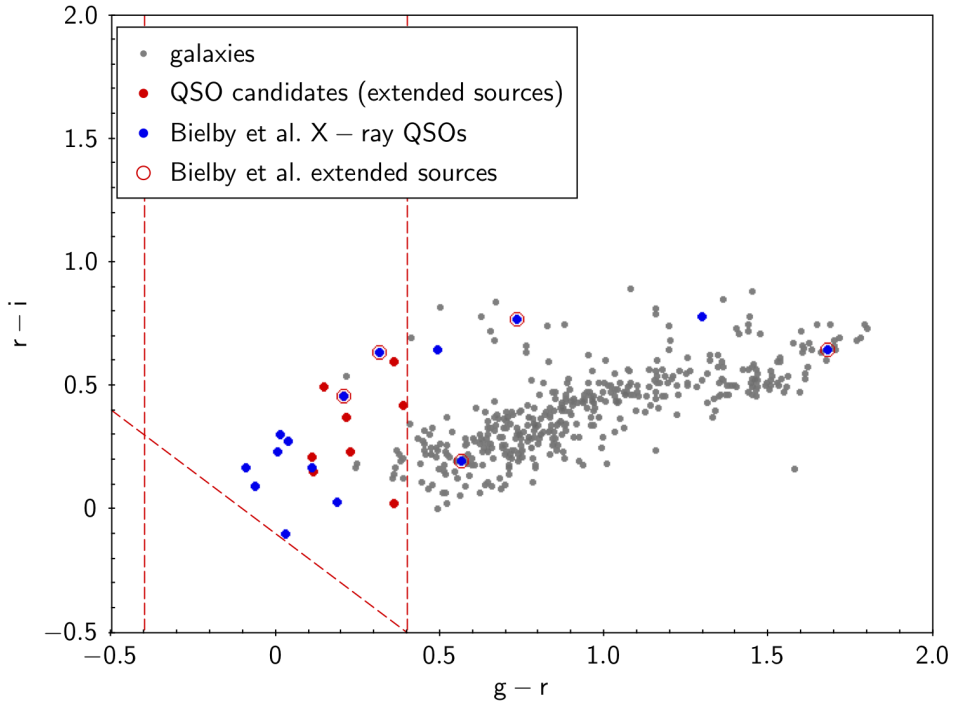

Figure 3.7: Colour selections performed on extended sources in the WHDF in the *gri* colour space. Extended sources (galaxies) are shown in gray. X-ray QSOs from Bielby et al. (2012) are shown in blue. The objects selected with our $ugr + giW1$ colour selections on objects classified as galaxies are shown in red. Our restricted cuts for galaxies are shown as red dashed lines.

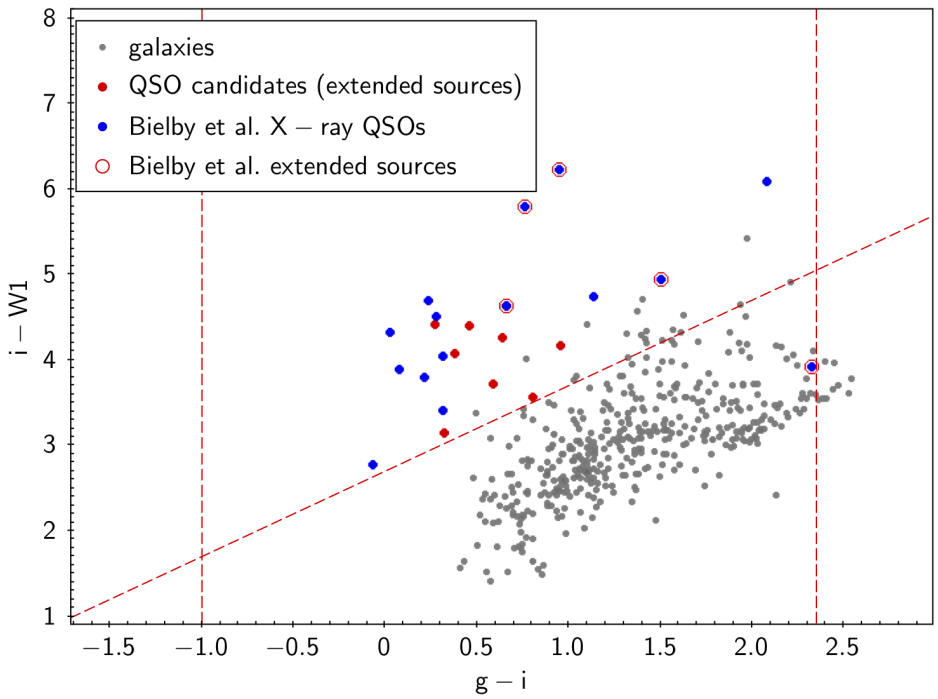

Figure 3.8: Colour selections performed on extended sources in the WHDF in the $giW1$ colour space. Extended sources (galaxies) are shown in gray. X-ray QSOs from Bielby et al. (2012) are shown in blue. The objects selected with our $ugr + giW1$ colour selections on objects classified as galaxies are shown in red. Our restricted cuts for galaxies are shown as red dashed lines.

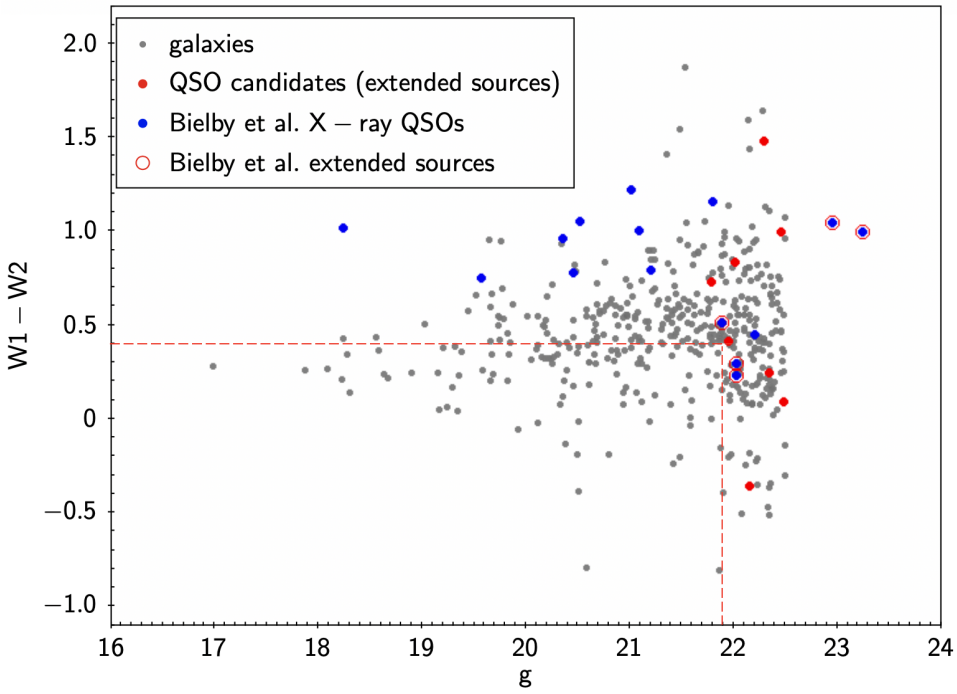

Figure 3.9: Colour selections performed on stellar sources in the extended WHDF in the $gW1W2$ colour space. Stars are shown in gray. X-ray QSOs from Bielby et al. (2012) are shown in blue. The objects selected with our $ugr+giW1$ colour selections on objects classified as stars are shown in green.

pleteness and efficiency of the $ugri$, $giW1$, and $ugri + giW1$ selections in the WHDF based on the 15 confirmed x-ray sources from Bielby et al. (2012). From this we get a stellar completeness of 80% with an efficiency of 73%. The selection including objects that have been possibly mis-classified as a galaxy yields a 66% completeness with 12% efficiency. However, as we checked the Chandra fluxes of the quasar candidates based on extended sources, we find that a likelier efficiency is 66%. Therefore, we believe that it is worth including a sample based on objects that may have been mis-classified as galaxies to increase completeness.

The full number counts of selected objects in the WHDF on both stellar sources and extended sources can be seen in Table 3.4. Here we notice a slightly different trend for the selections performed on stellar candidates v. galaxies, where the $ugri$ selection seems to cut down the number of galaxy candidates, but the $giW1$ selection cuts down the number of stellar candidates. Therefore a combination of both selections may be optimal.

From Table 3.2 we see that the X-ray absorbed quasars are WHDFCH007, WHDFCH008, WHDFCH044, and WHDFCH099. We see in our figures that WHDFCH008 is out of almost every colour cut we are making. Therefore, reddened objects such as that one may only be

Number Counts in WHDF for the colour selections					
Object Classification	total	ugri selection	giW1W2 selection	ugri+giW1W2	completeness
Stars (all Xray objects)	10	8	9	8	80%
Galaxies (all Xray objects)	5	4	5	4	80%
Stars ($g < 22.5$)	10	8	10	8	80%
Galaxies ($g < 22.5$)	3	2	2	2	66%

Table 3.3: Number counts with the colour selections applied on the X-ray quasars from Bielby et al. (2012).

WHDF Number Counts					
Object Classification	total	ugri selection	giW1W2 selection	ugri+giW1W2	efficiency
Stars	127	27	15	11	73%
Galaxies	438	13	27	9	12%

Table 3.4: Number counts for the WHDF *ugri* and *giW*1 selections. The total numbers reflect the number of stellar sources and extended sources in our magnitude range of $16 < g < 22.5$.

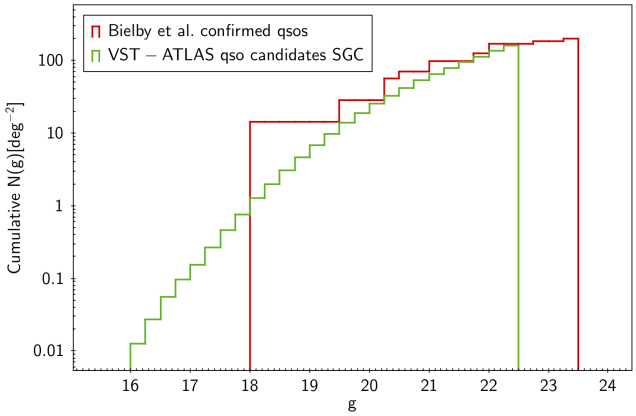

Figure 3.10: The quasar number counts per deg^2 in the SGC. Our quasar candidate number counts are shown in the green histogram. The cumulative quasar number counts calculated from the 15 Bielby et al. (2012) X-ray quasars are shown in pink.

picked up by X-ray surveys. We might expect extended sources that have X-rays to be lower redshift to be resolved, but the 5 Bielby X-ray sources that are morphologically classified as extended sources have a higher average redshift of $z = 1.35$ than the stellar sources, which have an average redshift of $z = 1.03$. As we can see in Fig. 3.9, the sources with a morphological classification as extended sources are fainter in g. As the morphology is robust to $g \sim 21$, these sources could be mis-classified.

3.3.3 WHDF Selection Summary and Conclusions

To summarize, testing our photometric selections in the extended WHDF area of ~ 0.071 deg^2, we find from Table 3.4 that the resulting catalogue of quasar candidates at $g < 22.5$ over the full VST-ATLAS data should have a quasar candidate sky density of ~ 155 deg^{-2}, based on the quasar candidates selected from stellar sources. If we include the colour selection with objects classified as galaxies, we have an upper quasar candidate sky density limit of ~ 281 deg^{-2}. Our estimate from WHDF based on the Bielby et al. (2012) detected X-ray quasars is that the actual quasar sky density is ~ 183 deg^{-2} if galaxies are included. This would imply a contamination of ~ 100 deg^{-2}, or 36%. From Fig. 3.10 we see that the WHDF quasar candidate number counts follow the trend of the spectroscopically confirmed quasar X-ray sources' cumulative sky density.

At our target magnitude of $g < 22.5$ we see from Table 3.1 that 10 of the X-ray sources are classified as stars and 3 are classified as galaxies. This means that a complete target selection would include $\sim 23\%$ galaxy candidates. In Table 3.2 we see that these objects are mostly at faint magnitudes of $g \approx 22$, where the morphological classification isn't as robust. Similarly, the visual analysis of the galaxy candidates as well as the Chandra fluxes support the possibility that these sources are mis-classified as galaxies. Overall, this would make it worthwhile to consider galaxies in our candidate selection.

3.4 VST-ATLAS Quasar Selection

We use the 2QDESp and WHDF analyses to create a photometrically selected quasar catalogue using VST-ATLAS+unWISE photometry. The initial colour selections from Chehade et al. (2016) are adjusted to restrict contamination while maximizing efficiency, based on both the WHDF selections and a 2QDESp analysis which is discussed in this section.

3.4.1 VST-ATLAS $ugri$ Selection

We show the ugr and gri selections for our VST-ATLAS sample in Fig. 3.11 and Fig. 3.12. By comparison with Fig. 3.1 we identify improvements we can make to the Chehade et al. (2016) cuts. Fig. 3.1 shows a group of sources without a positive identification circled in red at the edge of the main star sequence. We restrict the $u-g$ selection to decrease contamination from these objects and modify the original selections based on our WHDF analysis:

- $-0.5 \leq (u-g) \leq 0.65$
- $-0.4 \leq (g-r) \leq 1.1$
- $(r-i) \geq -0.1-(g-r)$

Additionally we use the following cuts:

- $(u-g) > 0.65$ & $(g-r) < -0.9*(u-g)+0.8$
- $(u-g) > 0.65$ & $(g-r) > 0.5*(u-g)$

In Fig. 3.11 and Fig. 3.12 we see the VST-ATLAS stellar locus in the $16 < g < 22.5$ magnitude range in gray. 2QDESp confirmed quasars are plotted in blue to show our high completeness in both areas. Our final quasar selection cuts are shown as green lines. In the ugr colour space, we clearly see the stellar main sequence as well as the red dwarfs, horizontal branch, and white dwarfs. Our cuts follow these main features to reduce stellar contamination. The diagonal cut in the gri colour space clearly reduces contamination from white dwarf stars.

3.4.2 VST-ATLAS $giW1W2$ Selection

We show the $giW1$ and $gW1W2$ selections for our VST-ATLAS sample in Fig. 3.13 and Fig. 3.14. By comparing with Fig. 3.1 and Fig. 3.4 we modify the $giW1$ selection to increase completeness of our quasar candidate selection. Additionally, we compare Fig.3.1 and Fig. 3.14 and identify a clear extended stellar locus. As our $W1$ and $W2$ photometric data from unWISE has improved depth, we notice less noise in the stellar locus in the $gW1W2$ colour space. Therefore, we extend the initial $W1-W2$ cut across our full $g-$band magnitude range rather than adjusting the cut at $g > 19.5$, as done by Chehade et al. (2016):

- $(i-W1) \geq (g-i)+1.5$

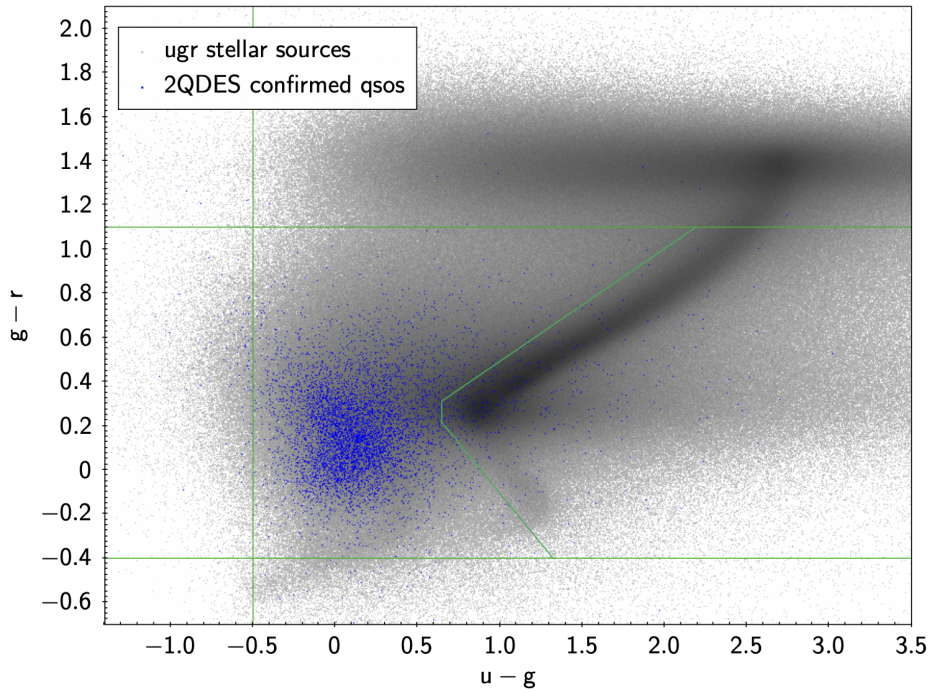

Figure 3.11: This figure shows 2QDES confirmed quasars in blue, stellar sources in gray, and our adjusted colour cuts are shown as green lines in the *ugr* colour space.

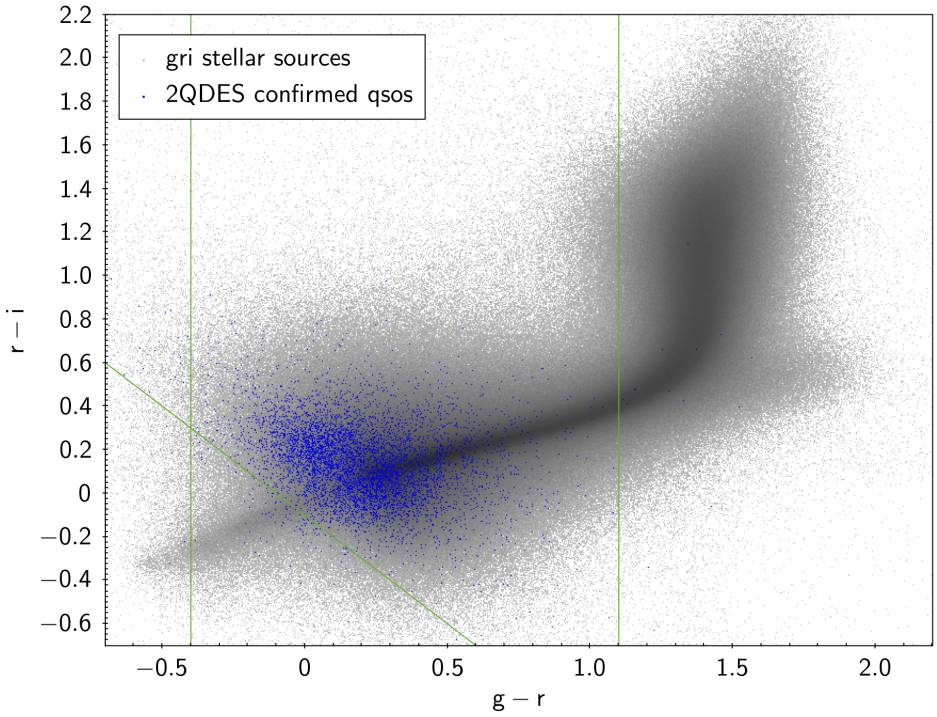

Figure 3.12: 2QDES confirmed quasars in blue are shown in blue, stellar sources in gray, and our adjusted colour cuts are shown as green lines in the *gri* colour space.

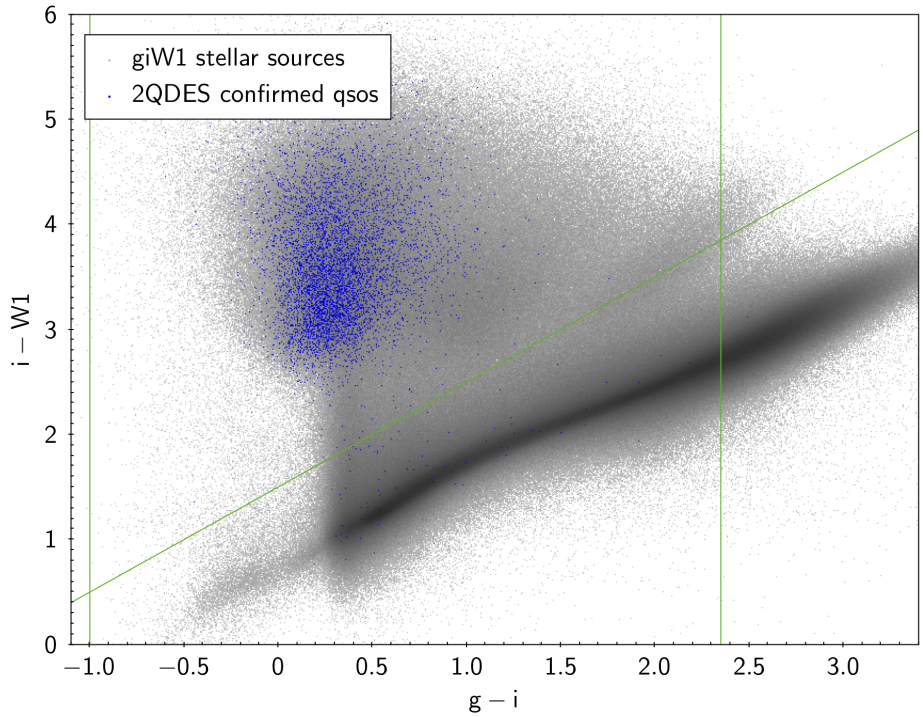

Figure 3.13: Here we plot 2QDES confirmed quasars in blue, stellar sources in gray, and our adjusted colour cuts are shown as green lines in the $giW1$ colour space.

- $-1 \leq (g - i) \leq 2.35$
- $(i - W1) \leq 8$
- $(W1 - W2) > 0.4$

In Fig. 3.13 and Fig. 3.14 we see the VST-ATLAS stellar locus in the $16 < g < 22.5$ magnitude range in gray. 2QDESp confirmed quasars are plotted in blue to show our high completeness in both areas. Our final quasar selection cuts are shown as green lines.

Comparison with DESI Selection

We check our selection criteria and colour cuts by comparing our adjusted VST-ATLAS+unWISE selections, based on those of Chehade et al. (2016) and our WHDF analysis, to the grz+WISE color-box selections outlined in DESI Collaboration et al. (2016). They state that the UVX property of quasars allows for the best separation between the stellar locus and quasars due to the bluer colours of quasars in the $u - r$ vs. $g - r$ colour space. However, in the absence of $u-$band photometry they rely on an optical-IR selection that utilizes the excess infrared emission of quasars to distinguish them from stars. The data used for this selection is a combination of the DECaLS $grz-$bands and NEOWISE $W1$ and $W2$ from the DR2 release.

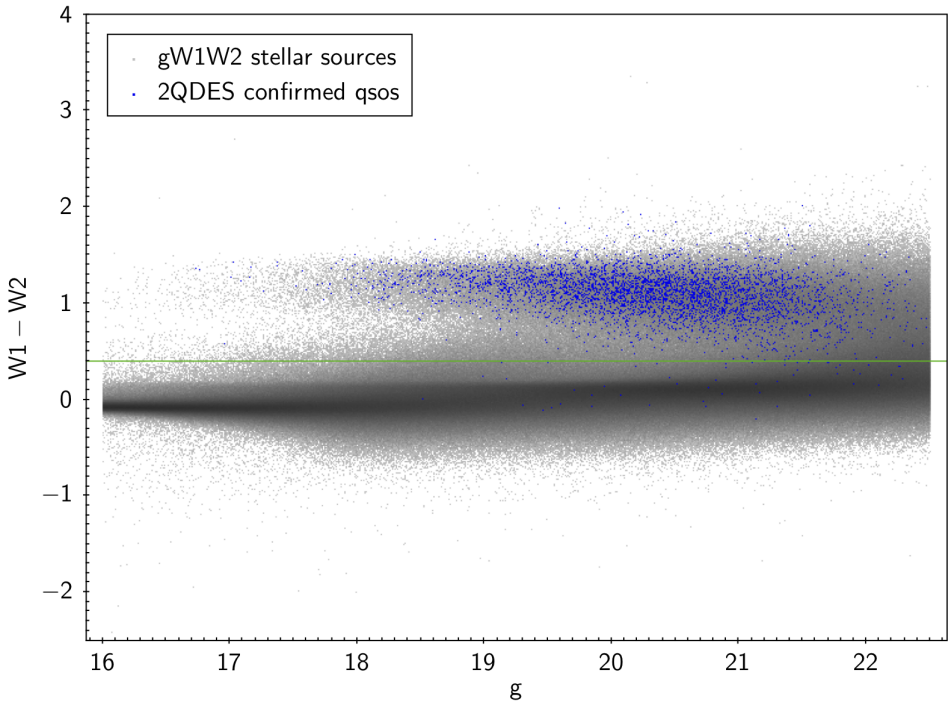

Figure 3.14: Here we plot 2QDES confirmed quasars in blue, stellar sources in gray, and our adjusted colour cuts are shown as green lines in the $gW1W2$ colour space.

In addition to cuts made in the $g-r$ vs. $r-z$ and $r-W$ vs. $g-z$ colour spaces (where $W = \frac{W1+W2}{2}$), they limit their target selection to $r < 23$ and use only objects classified as having a stellar morphology to reduce galaxy contamination. The $W1$ and $W2$ bands are probed deeper than the publicly available NEOWISE catalogue through Tractor-forced photometry, a technique developed by Dustin Lang which allows low signal-to-noise measurements to be utilized by fitting the different PSF from DESI and WISE to pixel-level data (DESI Collaboration et al. (2016)). These baseline selections are tested over an independent region of Stripe82. With the grz+WISE colour cuts, they expect a quasar sky density of $\sim$ 170 deg^{-2} from a candidate density of $\sim$ 260 deg^{-2}. This stellar contamination is cut down through a machine learning selection algorithm called Random Forest, which uses only color information to select quasars and was trained on all known quasars from DECaLS-DR2 (DESI Collaboration et al. (2016)).

First, to replicate the selections made by DESI Collaboration et al. (2016), we download a Sweep in this overlap area from the DECaLS Legacy Survey files DR7. The Sweep files are repackaged versions of the Tractor-forced catalogues each covering a $\sim$ 50 deg^2 area. To compare selection methods and data catalogues, we select a $\sim$ 7 deg^2 area in the SGC of our VST-ATLAS and unWISE data which has overlap with DECaLS DR7. Using the colour-cuts

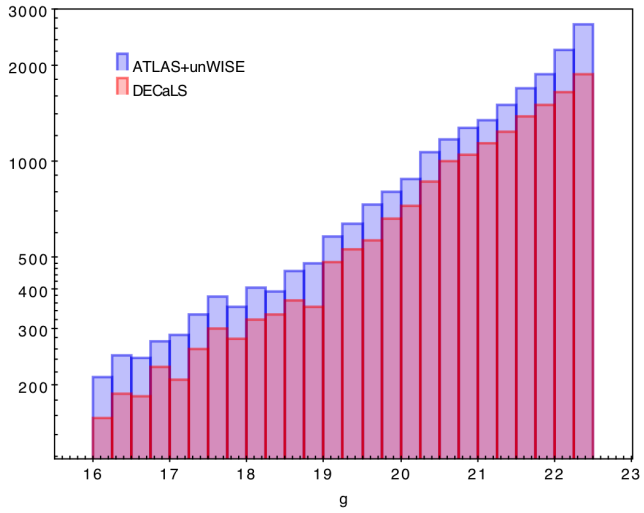

Figure 3.15: g-band stellar number counts in our target range of $16 < g < 22.5$ for the DECaLS and VST ATLAS data in a overlapping area of ~ 7 deg^2.

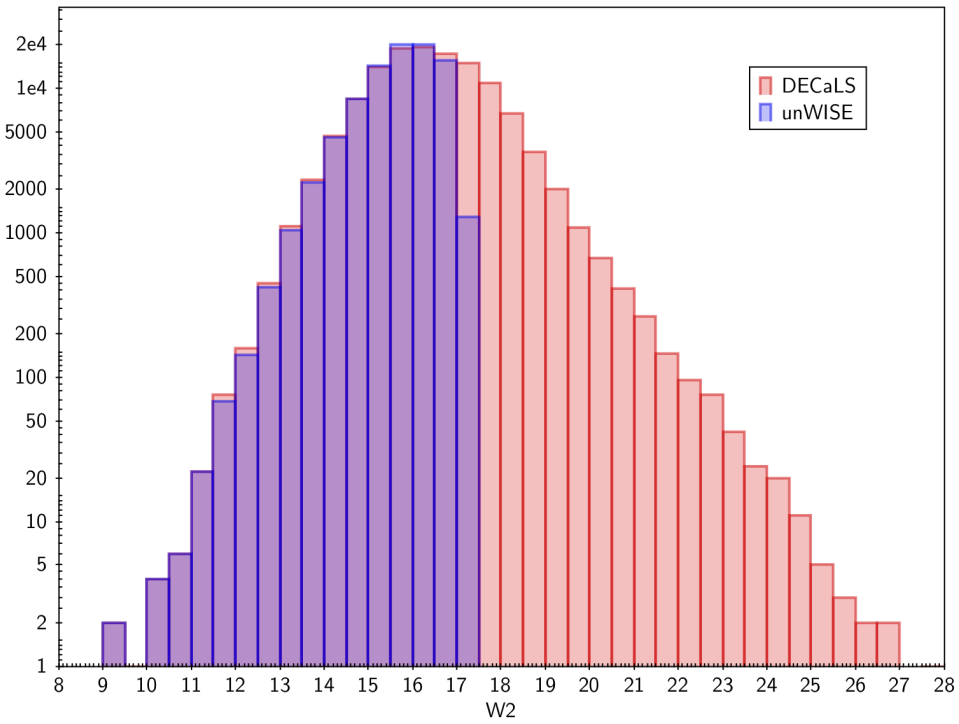

Figure 3.16: W2-band stellar number counts for $16 < g < 22.5$ in an overlapping region of the SGC. DECaLS number counts are shown in red and unWISE data is shown in blue.

outlined in Figure 3.16 of DESI Collaboration et al. (2016), we achieve a sky density of 285 deg^{-2} up to $g < 22.5$, which is the limit for our data. Therefore, we show that we can generate the candidates expected by the DESI collaboration on a newer data release (DR7 as opposed to DR2). We then use these same $grz + W1W2$ selections on our VST-ATLAS and unWISE data to compare the depths of the data and selection techniques.

Using the DESI Collaboration's photometric quasar candidate selections on our data (i.e. ATLAS+unWISE), we generate a quasar candidate sky density of ~ 143 deg^{-2}. Comparing our data to the DECaLS data, we find that up to the relevant limit of $g < 22.5$ they have similar number counts for stellar objects in the g-band (Fig. 3.15). Therefore the discrepancy from the 285 deg^{-2} sky density we achieve with the DECaLS data and the DESI Collaboration et al. (2016) selections to the 143 deg^{-2} sky density we achieve with the VST-ATLAS data and the DESI Collaboration et al. (2016) selections is most likely due to the Tractor-forced WISE photometry used by DESI. This gives them notably deeper W2 band data, as seen in Fig. 3.16.

To test this, we perform the DESI selections on our data, using only our $W1$ band (instead of a combination of $W1$ and $W2$) and get a candidate density of 230 deg^{-2}. We also perform the DESI selections on our data, but substitute in the Tractor-forced $W1$ and $W2$ band to get a 233 deg^{-2} sky density. Therefore, we see that using only the unWISE $W1$ band gives comparable results as using a combination of $W1$ and $W2$ TRACTOR-forced data from WISE. However, the sky density we achieve with both of these analyses is ~ 50 deg^{-2} less than the sky density we achieve with the DECaLS data.

As the photometric selection cuts used by Chehade et al. (2016) utilize the W2 band, as stated in Section 3.2, we test these selections again using only $W1$. In the ~ 7 deg^2 overlapping region, the $ugri + giW1$ cuts increase the number of VST-ATLAS quasar candidates to ~ 177 deg^{-2}, up from our original sky density of ~ 107 deg^{-2}. This gives us approximately the number of quasar targets as expected by DESI Collaboration et al. (2016). Of the additional ~ 70 deg^{-2}, most have W2 band detections in the DECaLS data, but not in ATLAS. Therefore, we can see that $\sim$ half of these candidates fall below our original combined $W1 - W2 > 0.4$ cut. From this we can assume that $\sim 50\%$ of the additional quasar candidates are stellar contamination. Therefore we have ~ 177 deg^{-2} candidates including ~ 35 deg^{-2} contamination.

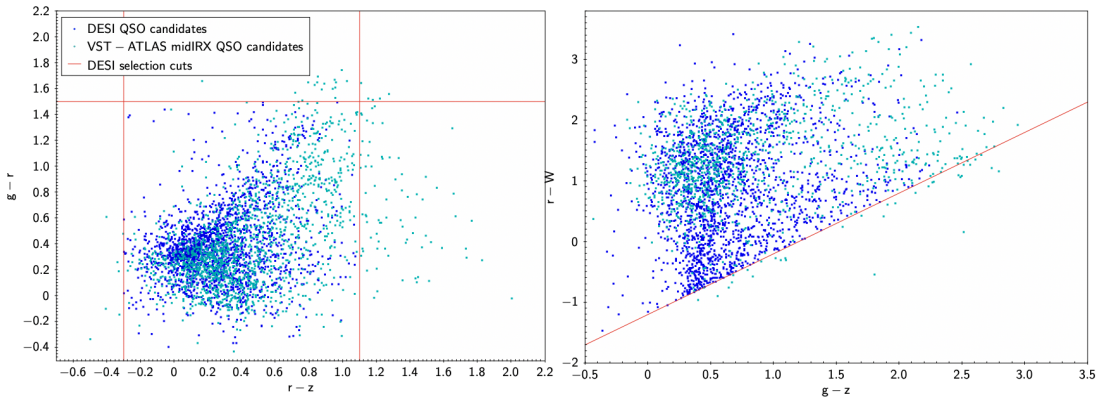

Figure 3.17: Quasar candidates in the $r-z$ v. $g-r$ colour space and the $g-z$ v. $r-W$ colour space in a 7 deg^2 overlap with DECaLS. The blue points represent quasar candidates selected using the cuts outlined by DESI Collaboration et al. (2016). The teal points are quasar candidates selected through our mid-IR colour selections. The red lines show the cuts used by DESI Collaboration et al. (2016).

DESI Selection - $grzW$ vs. $giW1$

In the overlapping area, we compare the DESI selection methods on the DECaLS data to our selection methods on the ATLAS+unWISE data. The number densities of quasar candidates as a result of the DESI mid-IR selection methods are very similar to the number densities we find using our mid-IR $giW1$ cuts only (without the W2 band). We find ~ 288 candidates deg^{-2} (compared to the 285 deg^{-2} selected by DESI methods), covering similar areas in the colour spaces as the DESI selections. These overlapping selections can be seen in Fig. 3.17. Therefore, as postulated by DESI2016, our UVX selection appears to cut down stellar contamination in the quasar candidate selection.

3.4.3 VST-ATLAS $ugri + giW1$ Selections

To test the completeness and efficiency of the $ugri + giW1$ cuts we have determined from our WHDF and DESI analysis, we look at a high density area of the 2QDESp survey from Chehade et al. (2016), which includes an area with ~ 72 deg^{-2} QSO candidates to $g < 22.5$. As shown in Table 3.5, over our full $16 < g < 22.5$ selection we have a stellar candidate completeness of 86%, with an efficiency of 28%. However, we take into account that throughout the 2QDESp survey there was high spectroscopic completion to $g < 21$. Therefore, we look at our survey to $g < 21$ and then the $21 < g < 22.5$ area to see if we will have to adjust

ATLAS v. 2QDES Test Area Stellar Number Counts					
Object Classification	total	ugr selection	giW1 selection	ugr+giW1	completeness and efficiency
Stars	46028	3254	3908	2409	efficiency 28%
2QDES QSOs	747	632	710	645	completeness 86%

Table 3.5: Number counts in the 2QDES test area with the colour selections applied on all objects classified as stellar sources in the g or r band. Total number counts are objects within our magnitude range of $16 < g < 22.5$.

ATLAS v. 2QDES Test Area Number Counts g-band Limits					
Object Classification	total	ugr selection	giW1 selection	ugr+giW1	completeness and efficiency
Stars ($g < 21$)	25456	3844	1238	852	efficiency 53%
2QDES star QSOs ($g < 21$)	481	452	473	449	completeness 93%
Stars ($21 < g < 22.5$)	20572	3664	2670	1561	efficiency 12.6%
2QDES star QSOs ($21 < g < 22.5$)	260	203	239	197	completeness 76%

Table 3.6: Number counts in the SGC with the colour selections applied on all objects classified as extended sources in the g and r band. Total number counts are objects within our magnitude range of $16 < g < 22.5$.

our colour-colour space selections to account for the increase in noise as we probe deeper data. Table 3.6 shows that to a limit of $g < 21$ we have a target completeness of 93%. In the magnitude limit from $21 < g < 22.5$ we have a completeness of 76%. Here we also see that the most contamination comes from the stellar selection at $21 < g < 22.5$. Therefore, to reduce contamination in our sample, we could perform different selections at faint magnitudes. However, this contamination is tricky to test due to the spectroscopic incompleteness of 2QDESp at $g > 21$. We expect much more complete results in the $21 < g < 22.5$ magnitude range with our survey. Therefore, the completeness and efficiency of our catalogue at $g < 21$ when compared to the 2QDESp survey is most informative and important.

3.5 Final ATLAS Photometric Selections

We finalize our quasar selection by utilizing known photometric cuts based on the UVX and IR excess emission properties of quasars. We perform an analysis on the WHDF to see how X-ray selected quasars can further inform our selection and determine that a cut which in-

cludes objects classified as galaxies should be added to increase completeness. We then check these cuts against the photometric selections used by DESI Collaboration et al. (2016) to conclude that our W2 band cut should be eliminated. Our final quasar candidate counts (before the addition of the $ugr + giW1$ cut on galaxies) in the NGC give us a sky density of 185 deg^{-2}, and a sky density of 162 deg^{-2} in the SGC. The colour selections performed on galaxies give an additional candidate sky density of 35 deg^{-2}. Over the whole Southern sky this gives us a candidate sky density of 170 deg^{-2} with just stellar candidates and a candidate sky density of 204 deg^{-2} with the additional galaxy selections.

From our WHDF analysis we get a 75% completeness and 65% efficiency. The 2QDES analysis gives us 92% completeness and 56% efficiency. Therefore, we can assume a total 85% completeness and 60% efficiency across the Southern sky for our full catalogue. From our stellar selection, this would mean a quasar sky density of $\sim$ 100 deg^{-2} with a stellar contamination of $\sim$ 70 deg^{-2}. From the miss-classified galaxies, we can then assume a quasar candidate sky density of $\sim$ 20 deg^{-2} with a galaxy contamination of $\sim$ 15 deg^{-2}. Combining both of these selections gives us a final quasar sky density of $\sim$ 120 deg^{-2} from a candidate sky density of 204 deg^{-2}. This is close to our target of 130 deg^{-2}.

Chapter 4

Final VST ATLAS QSO Catalogue

4.1 VST-ATLAS QSO CATALOGUE

Using the $ugri + giW1$ colour selections we determined in Chapter 3, we generate our photometrically selected VST-ATLAS quasar catalogue. The full number counts for both the UVX and mid-IRX selections are shown in Table 4.1. Our final photometric selections can be seen in Fig. 4.1, Fig. 4.2, and Fig. 4.3. In these figures, objects identified as stellar sources in the $g-$ or $r-$ bands (between $16 < g < 22.5$) are plotted in light gray. Our final quasar candidates are shown as a density gradient in pink and blue, with higher density areas being blue, and our selection cuts are shown as green lines.

Over the whole $\sim$ 4000 deg^2 area covered by VST-ATLAS and unWISE in the Southern Hemisphere, the combination of our $ugri$ and $giW1$ selections on stellar sources give us a sky density of $\sim$ 170 deg^{-2} quasar candidates. The $ugri$ selection on its own gives us a sky density of $\sim$ 616 deg^{-2}. The mid-IR $giW1$ selections give us a sky density of $\sim$ 329 deg^{-2}. The addition of galaxies increases that sky density to $\sim$ 204 deg^{-2}. As stated in Section 3.5, we assume a complenetess of 85% and efficiency of 60%, giving us a final quasar sky density of $\sim$ 120 deg^{-2}.

4.1.1 Maps

The quasar candidate sky density across the NGC and SGC is relatively uniform, barring some striping most likely due to sky conditions, as can be seen in Fig. 4.4 and Fig. 4.5. The

Full Southern Hemisphere Number Counts					
Object Classification	total	ugri selection	giW1 selection	ugr+giW1	sky density (deg^{-2})
Stars	18254560	2553913	1362143	703669	~ 170
Galaxies	15466641	421452	2374893	142774	~ 34
Combined	33721201	2975365	3737036	846443	~ 204

Table 4.1: Number counts in the SGC with the colour selections applied on all objects classified as stellar sources in the g or r band, and the restricted cuts on objects classified as extended sources in the g and r band. The total number counts reflect the number counts for objects that are in ourj in our magnitude range of $16 < g < 22.5$.

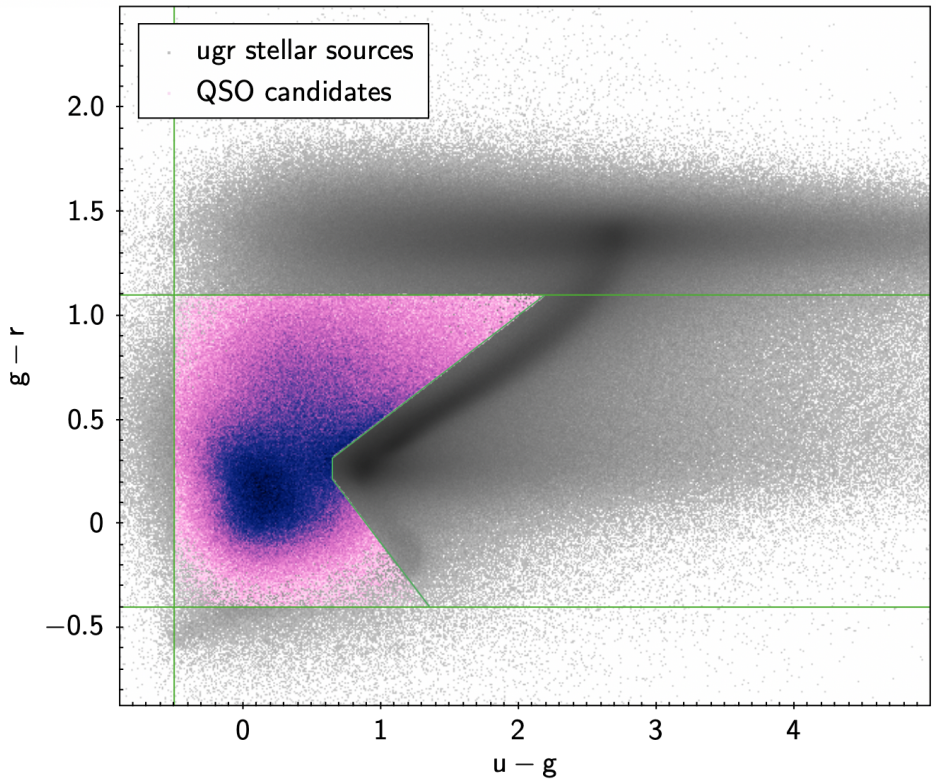

Figure 4.1: Colour selections performed on the VST-ATLAS data in the ugr colour space. Stellar sources are shown in gray. Our quasar candidates selected with the $ugr+giW1$ colour cuts are shown as pink and blue points. The pink to blue gradient denotes a higher density of candidates in the blue space.

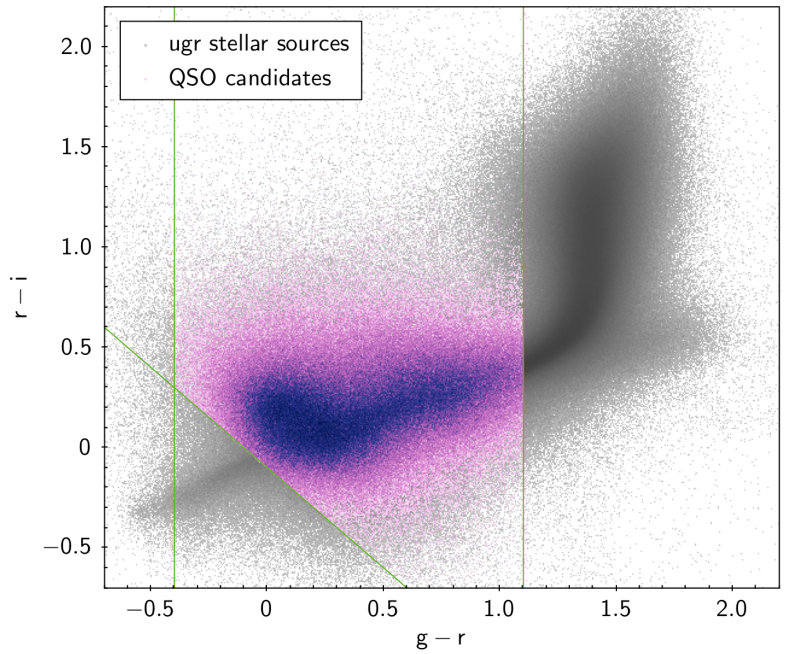

Figure 4.2: Colour selections performed on the VST-ATLAS data in the *gri* colour space. Stellar sources are shown in gray. Our quasar candidates selected with the $ugr + giW1$ colour cuts are shown as pink and blue points. The pick to blue gradient denotes a higher density of candidates in the blue space.

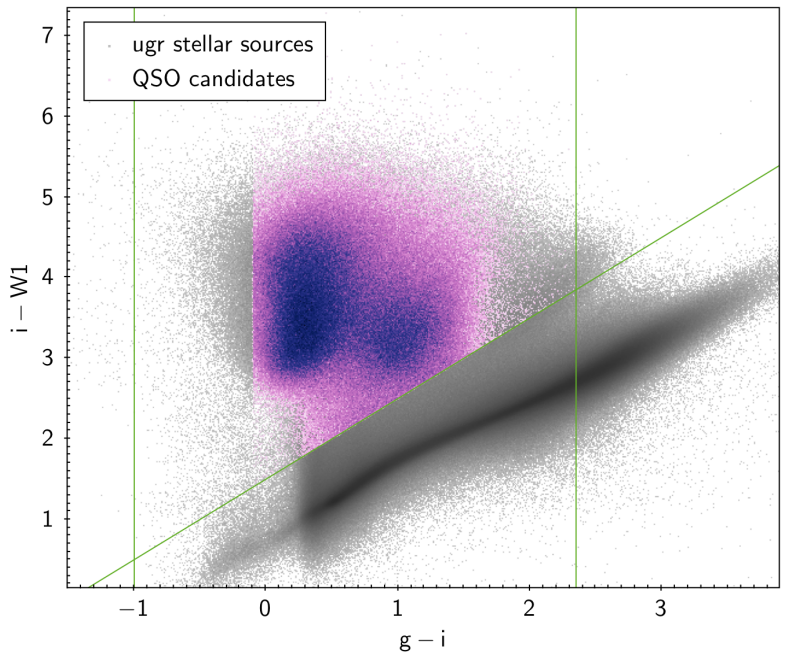

Figure 4.3: Colour selections performed on the VST-ATLASunWISE data in the $giW1$ colour space. Stellar sources are shown in gray. Our quasar candidates selected with the $ugr + giW1$ colour cuts are shown as pink and blue points. The pick to blue gradient denotes a higher density of candidates in the blue space.

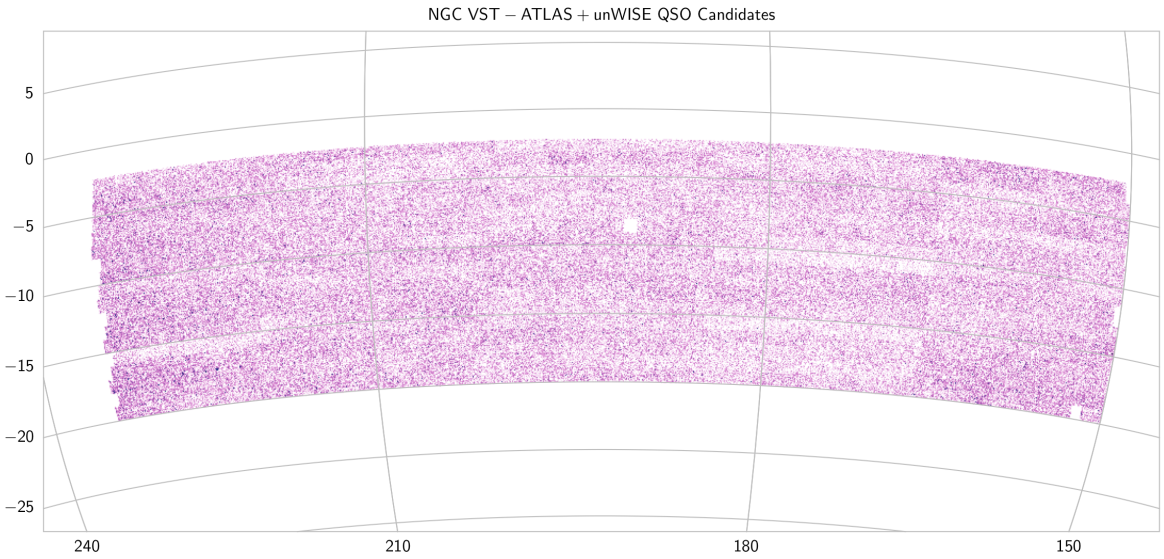

Figure 4.4: Sky density of selected quasar candidates in the NGC for $16 < g < 22.5$

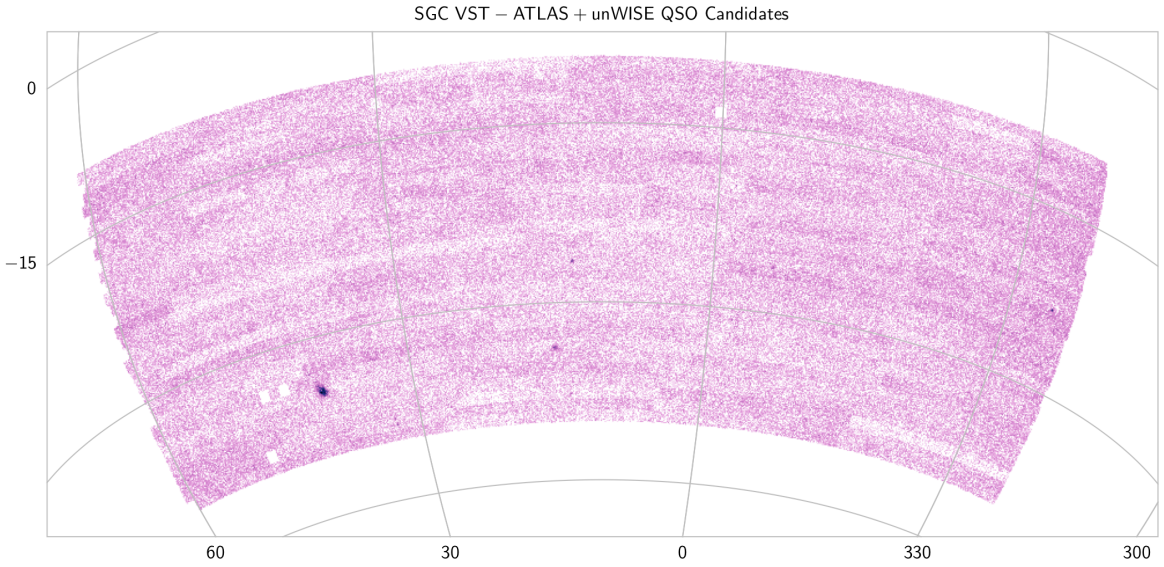

Figure 4.5: Sky density of selected quasar candidates in the SGC to $16 < g < 22.5$

lower density areas, which are shown as white areas in the Figures, are masked out in the statistical analyses performed in the next sections of this paper.

4.1.2 n(g)

The majority of our candidates are at $21 < g < 22.5$, which is a depth that has previously not been probed at such large scales in the Southern Hemisphere. To show this increased depth we are able to probe with VST ATLAS and UNWISE, we show the number of candidates in the g-band in Fig. 4.6. Here we see that the addition of candidates morphologically classified as galaxies gives a slight increase in $g-$band number counts at $g >\sim 20.5$.

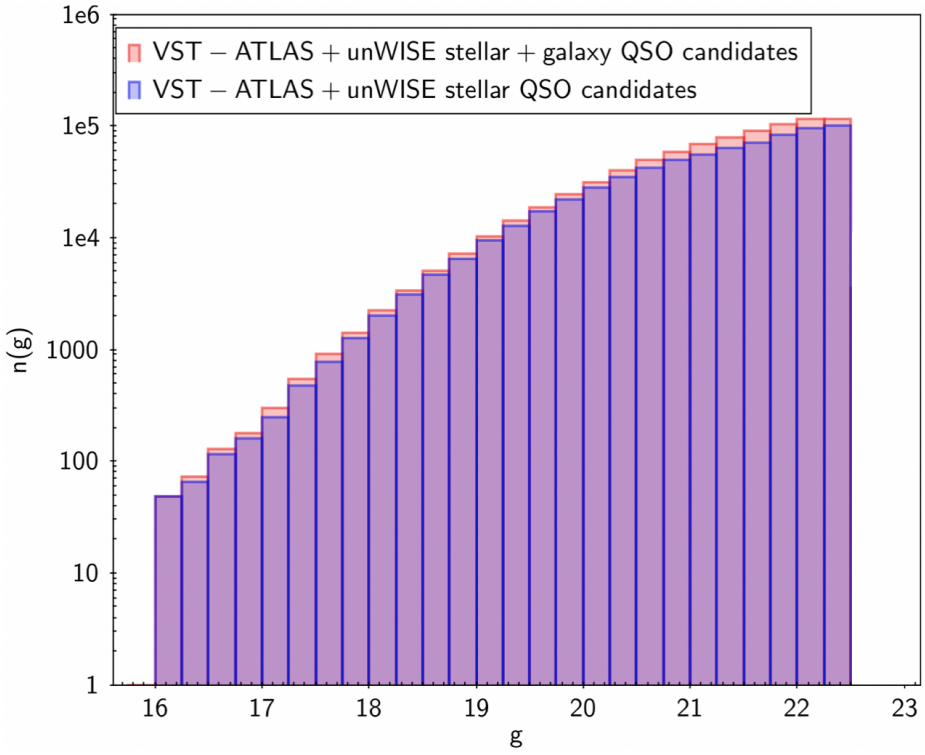

Figure 4.6: Histogram of g-band values of our full VST-ATLAS QSO catalogue.

We compare with WHDF data as discussed in the previous chapter, see Fig. 3.10, to show that our number counts in this fainter $g-$band magnitude region follow the expected number counts from the confirmed X-ray quasars in the 0.071 deg^2 WHDF area.

We show a further comparison of $g-$band quasar candidate number counts by looking at the work done in Palanque-Delabrouille et al. (2016). They present a new measurement of the quasar luminosity function (QLF) using data from the extended Baryon Oscillation Spectrocopic Survey (eBOSS) in the redshift range $0.68 < z < 4.0$. This data is fit by a double power-law model, with a linear pure luminosity-function (PLE) for redshifts of $z < 2.2$ combined with a luminosity and density evolution model (LEDE) at $z > 2.2$. This new QLF is measured to to find the expected quasar number counts in order to optimize the fiber targeting for DESI, which is aiming to reach limiting magnitudes of $g \sim 23$. They update their selection algorithm based on the time variability of quasar fluxes instead of using a photometric selection method as the number density of quasars at $z < 0.9$ and $z > 2$ decreases, making photometric selections less efficient. Therefore we want to see how our photometrically selected catalogue of quasar candidates compares to the selection method based on the

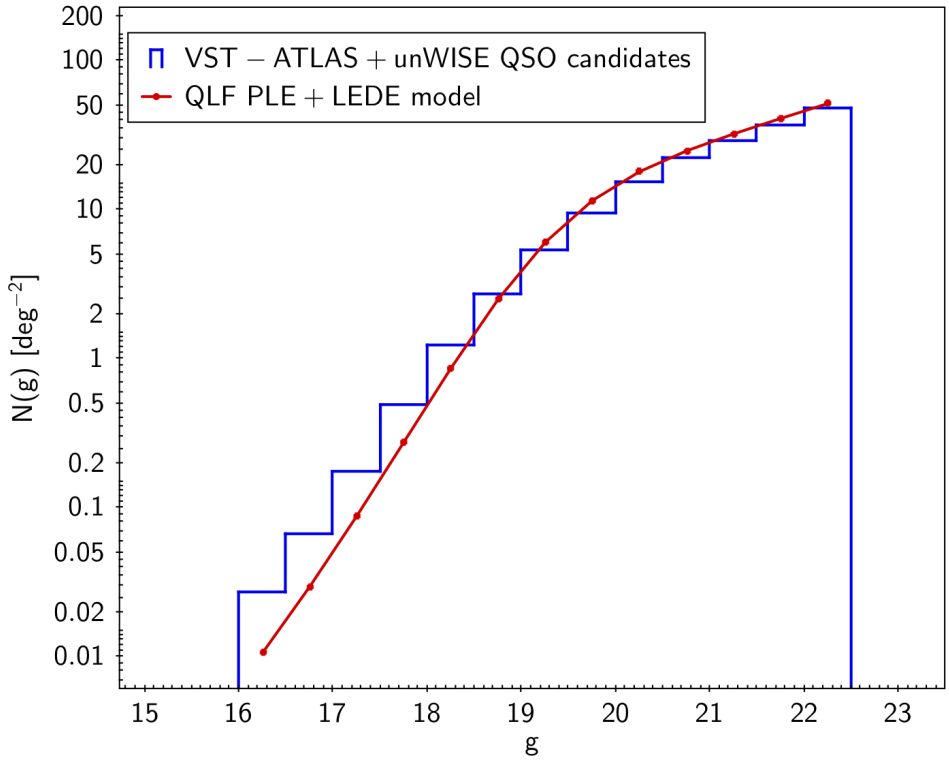

Figure 4.7: The VST-ATLAS+unWISE quasar candidate number counts per deg^2 as a function of $g-$band magnitude are shown in the blue histogram. The expected quasar number counts calculated from the QLF PLE+LEDE model in the $0 < z < 3$ redshift range from Palanque-Delabrouille et al (2016) are shown in red.

quasar luminosity function, in a redshift range where the number density of quasars hasn't decreased enough to create problems.

From Table 6 of Palanque-Delabrouille et al. (2016), we take the expected quasar number counts, which are presented in bins of $\Delta g = 0.5$ and $\Delta z = 1$ for the magnitude range of $16 < g < 22.5$ and the redshift range of $0 < z < 3$. These expected number counts are plotted as red points in Fig. 4.7. They predict a quasar candidate sky density of 195 deg^{-2} over their full redshift range at $g < 22.5$.

Our quasar selection gives a candidate sky density of 204 deg^{-2} at $g < 22.5$. We have agreement to within $\sim 5\%$ with the Palanque-Delabrouille et al. (2016) QLF PLE+LEDE model over their redshift range of $0 < z < 3$. However we have to account for contamination in our sample. We use Figure 12 in Palanque-Delabrouille et al. (2016) to estimate number counts in our redshift range as opposed to the $0 < z < 3$ which we can take from Table 6, as the data is presented in bins of $\Delta g = 0.5$ and $\Delta z = 1$. From Figure 12 in Palanque-Delabrouille

et al. (2016), we can calculate a rough quasar candidate sky density in our redshift range as they present the redshift distribution of candidates generated by their model in $\Delta z = 0.2$ bins. Therefore, from the 195 $\deg^{-2}$ candidates at $z < 3$, we find $\sim 141\deg^{-2}$ in the redshift range of $0.8 < z < 2.4$. This means that 75% of candidates generated from the PLE+LEDE model in the $0 < z < 3$ redshift range should be found in our quasar candidate catalogue.

4.2 ANNz2 Photometric Redshift Estimation

To determine the redshift of the candidates in our quasar catalogue we utilize ANNz2, a software for photometric redshift (photo-z) estimation, presented by Sadeh et al. (2016). This code uses artificial neural networks and boosted decision/regression trees to optimize the photo-z estimation and has already been implemented as part of the analysis in the Dark Energy Survey. ANNz2 utilizes training based machine learning methods to derive the relationship between photometric observables and redshift.

4.2.1 ANNz2 Training

To use ANNz2, we must train the algorithm with existing data which has similar properties to our candidates. We generate a training catalogue with 19716 objects from a combination of spectroscopically confirmed eBOSS, 2QDES, and 2QZ quasars found in areas of the NGC and SGC which overlap with our VST-ATLAS+unWISE catalogue. The spectroscopic redshift distribution of the quasars in this training sample is shown in Fig. 4.8. We use the $ugrizW1W2$ magnitudes, errors, and spectroscopic redshifts of these samples to train the algorithm as these confirmed quasars were targeted through similar colour selections and are in a redshift range close to our target of $0.7 < z < 2.3$.

To test the efficiency of the algorithm as well as our training sample, we choose a random sample of the training catalogue to be used as the training sample in the code. We test the results of this training on the remainder of the training catalogue, for which we have known redshifts. The result of that is seen in Fig. 4.9. Here we plot the photometric redshift estimated by ANNz2 vs. the spectroscopic redshift of the training sample. We can compare our results with the photo-z regression algorithm presented in Yang et al. (2017). They found that the best method to estimate photo-z was the Skew-t method which gave them 74.2% of

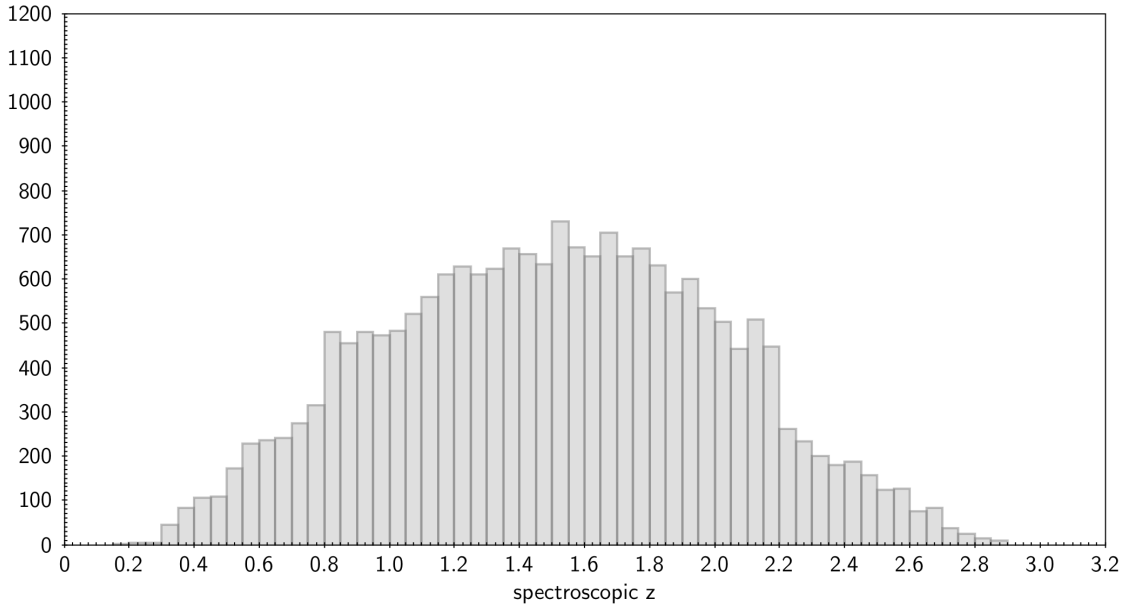

Figure 4.8: Spectroscopic reshift distribution of our ANNz2 training sample.

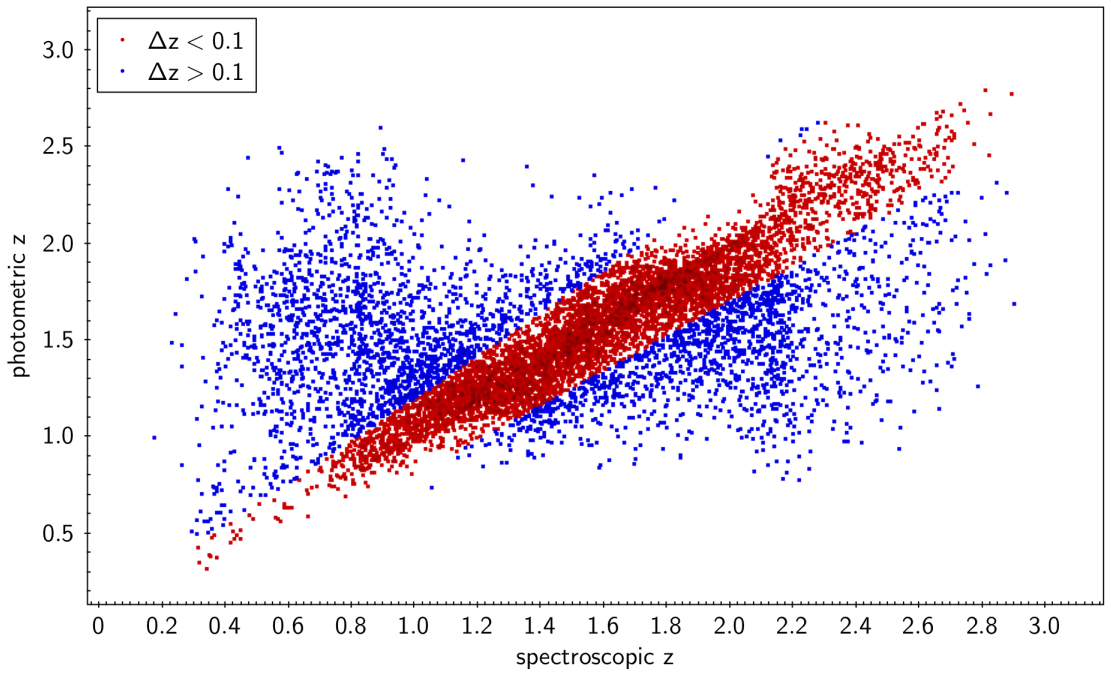

Figure 4.9: Photometric redshift compared to spectroscopic redshift for a random half of our training sample using the ANNz2 algorithm. Outliers are shown in blue.

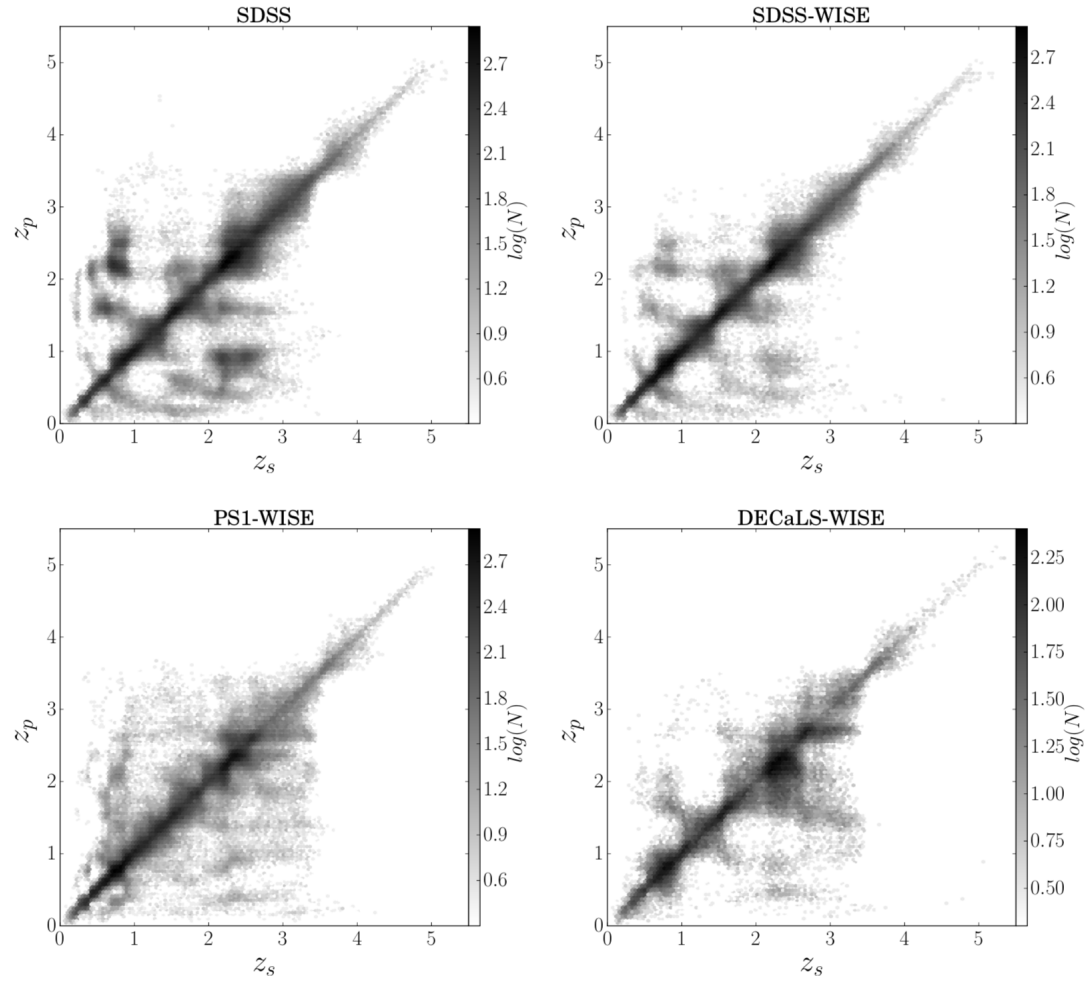

Figure 4.10: Photometric redshift estimations vs. spectroscopic redshift using the Yang et al. (2017) photo-z regression algorithm.

objects within $\Delta z < 0.1$. To check the efficiency of our ANNz2 method, we remove outliers in the training sample by implementing the following cut (shown as blue points in the figures):

$$\frac{|z_{photo} - z_{spec}|}{1 + z_{spec}} > 0.10$$

From this we see that 64% or our results are within $\Delta z < 0.1$, with a standard deviation of 0.18. Once we remove the 36% outliers, we see that the standard deviation of our photo-z estimation is 0.0275. Removing outliers gives us a better estimate of the underlying error, i.e. the limiting redshift error that may be available from this data.

The relative degeneracy of the photometric redshift approximations in our redshift range of $0.7 < z < 2.3$ can also be seen in the work done by Yang et al. (2017), as shown in Fig. 4.10. This figure is taken from their Figure 4. It shows the results of their photo-z

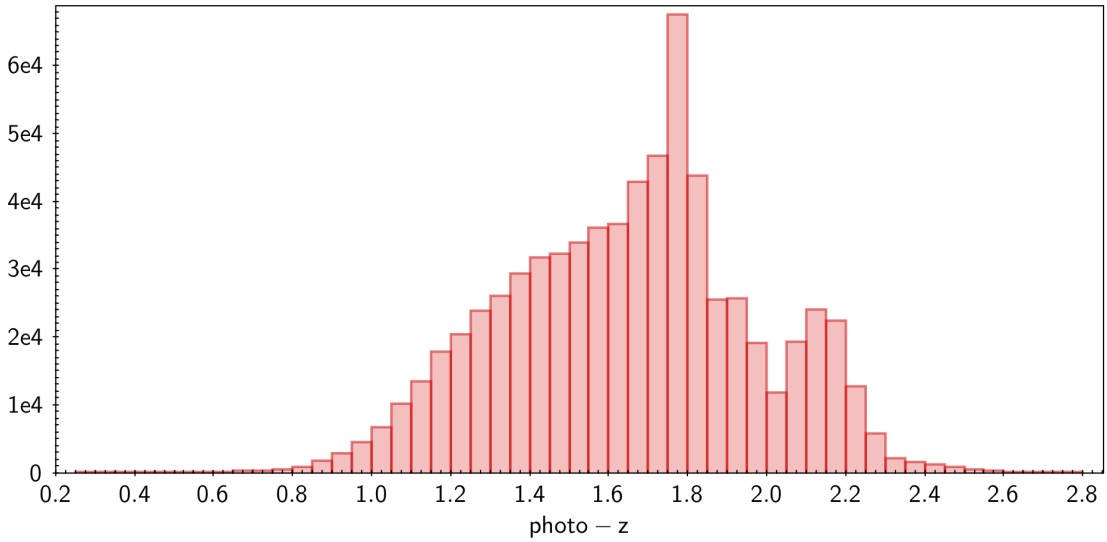

Figure 4.11: Photo-z distribution of our full quasar candidate catalogue

regression algorithm performed on photometric data from SDSS, SDSS+WISE, PS1+WISE, and DECaLS+WISE. This also shows that a combination of optical and MIR photometric data increases the accuracy of the photo-z estimations. The increased efficiency of their photo-z estimations may also be due to the inclusion of the $3 < z < 5$ redshift range.

The redshift distribution of our quasar candidates, as calculated by the ANNz2 code, can be seen in Fig. 4.11. We notice a spike at $z \sim 1.8$ as well as a slight decrease in number counts at $z \sim 2.0$. Future inclusion of other bands such as J and K may be needed to address such degeneracies and reduce the number of photo-z outliers.

4.3 Final QSO Catalogue Conclusions

Here have presented the full VST ATLAS Quasar Survey, including initial photometric redshifts using the ANNz2 algorithm. We also perform a $g-$band number count comparison with the work done in Palanque-Delabrouille et al. (2016) as these models are used by DESI Collaboration et al. (2016) to determine their expected quasar number counts. Therefore, we are able to compare our photometric selection method to the model number count based on the quasar luminosity function, finding good agreement between the two. However, we must take into account expected stellar contamination in our sample as well as an adjusted expected number count from the QLF model due to the reduced reshift range we are probing. Therefore our quasar counts may still be more contaminated with stars than currently

estimated and this requires further testing.

We have constructed our VST ATLAS quasar survey to use ultimately with the eROSITA and 4MOST quasar surveys. The survey gets close to our target sky density for competitive BAO work at $z \approx 1.7$ reaching $120\mathrm{deg}^{-2}$ at $g < 22.5$. Improvements to our quasar selection including deeper $u-$band as well as deeper NEOWISE data and also eROSITA X-ray data mean that we are well positioned to reach or exceed our target sky density of $130\mathrm{deg}^{-2}$. Meanwhile these and further improvements such as the inclusion of the J and K bands from VHS etc will hopefully reduce the errors on our quasar photometric redshifts. In the next chapters we shall exploit the current quasar catalogue for galaxy-quasar and quasar-CMB lensing cross-correlations. Although we shall use a conservative version of the quasar catalogue for these applications, their success or otherwise should also provide the first independent evidence of the overall quality of the VST ATLAS Quasar Survey.

Chapter 5

QSO - Galaxy Lensing

5.1 Introduction

We can perform a weak gravitational lensing analysis through a cross-correlation of background quasars and foreground galaxies and galaxy clusters. This cross-correlation is a powerful probe of the masses of galaxies, galaxy groups, and galaxy clusters. The distortion of these background objects by large scale structures can also help constrain cosmological parameters. Previous works by Myers et al. (2003), Myers et al. (2005) and Mountrichas & Shanks (2007) have used background 2dF quasars to detect the effect of galaxy and galaxy cluster lensing and Scranton et al. (2005) have performed such lensing analyses using photo-z selected quasars from SDSS. Myers et al. (2003) and Mountrichas & Shanks (2007) argue that their results imply a high Ω_M and/or strong anti-bias, and are therefore inconsistent with the standard Λ Cold Dark Matter (ΛCDM) model. However, Scranton et al. (2005) argue that their results are compatible with the standard ΛCDM model.

We look for the lensing of background quasars by foreground galaxy clusters and individual galaxies. This lensing is defined as the gravitational deflection of photons (bending of light) around large masses, which causes a magnification of background sources (Scranton et al. (2005)). The magnification causes the background objects to appear brighter than they actually are and it reduces the surface density of background objects. Here we present our results and their interpretations, and then discuss the implication for the cosmological model of these results. We present observational results to show that an anti-correlation is detected at faint quasar magnitudes and a positive correlation at detected at bright magnitudes as

predicted by lensing.

5.2 Cross-Correlation Data Catalogues

5.2.1 Quasar Sample

The VST-ATLAS quasar catalogue described in Chapter 4 has a certain amount of stellar and galaxy contamination to improve completeness. To perform these weak lensing analyses we use a more conservative, point-source only selection of our quasar catalogue to reduce galaxy contamination as well as possible overlap in the galaxy and quasar catalogues. We use the quasar candidate catalogue with the $ugri + giW1W2$ cuts described in Section 3.4.1 and Section 3.4.2. We then further restrict this stellar candidate selection is to $g < 22$. Of this more conservative selection, we only consider quasar candidates with photometric redshifts $z > 1$ to prevent overlap in real space of quasar and galaxy samples, using results from the ANNz2 photometric redshift estimation. These selections result in a total of 336905 objects giving us a quasar candidate sky density of 81deg^{-2}.

5.2.2 Galaxy Cluster Sample

We use the VST ATLAS Southern Galaxy Cluster Catalogue (Ansarinejad et al. (2019, in prep)) to perform the angular cross-correlations between foreground galaxy clusters and background quasars. The galaxy groups and clusters in this catalogue were selected using VST ATLAS optical photometry in the *griz* bands using the ORCA cluster detection algorithm. The ORCA cluster detection algorithm (Murphy et al. (2012)) finds similarities in galaxy colors and regions with a high projected surface density and then uses the Friends of Friends technique to determine galaxy clusters groups. The selection criteria is described in full in Ansarinejad et al. (2019, in prep). This cluster catalogue overlaps the full ~ 4000 deg^2 area of our VST-ATLAS quasar survey.

As Myers et al. (2003) present a cross-correlation between galaxy cluster catalogues and their quasar sample, we introduce similar selections into our galaxy cluster catalogue in order to compare our results. Myers et al. (2003) use photometrically selected galaxy catalogues from the APM Galaxy Survey and the Early Data Release of Sloan Digital Sky Survey with a limiting magnitude of B= 20.5. They generate friends-of-friends galaxy clusters by determining

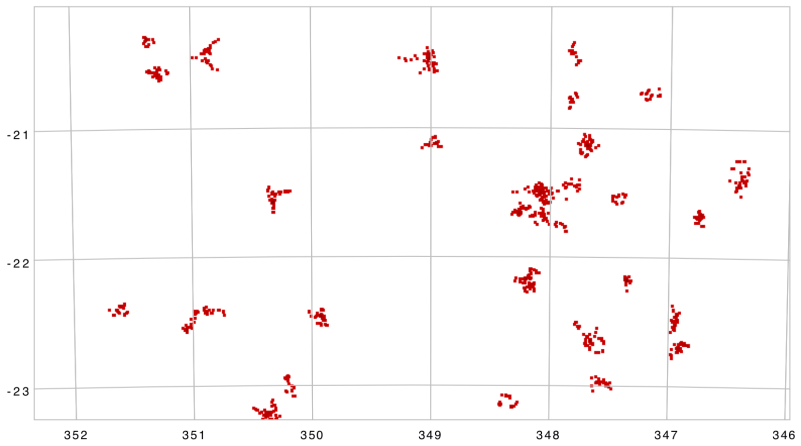

Figure 5.1: Sky map of defined $n \geq 14$ galaxy clusters in a section of the SGC with each point corresponding to a galaxy.

the overdensity parameter $\delta = 8$ and define the minimum group size as a cluster with 7 or more members ($n \geq 7$). They state that this minimum group member value is chosen as a smaller group might incur contamination from galaxies being grouped together due to their alignment at different redshifts.

We therefore introduce a magnitude cut at $g < 20.5$ in our galaxy cluster catalogue to be able to compare our results to Myers et al. (2003). This galaxy cluster catalogue is then divided into clusters with 5 or more members ($n \geq 5$), clusters with 7 or more members ($n \geq 7$), and clusters with 14 or more members ($n \geq 14$). The resulting $n \geq 5$ catalogue has $N_g = 96915$, with a galaxy cluster sky density of 2.46deg^{-2}. The $n \geq 7$ catalogue has $N_g = 69758$, with a galaxy cluster sky density of 1.24deg^{-2}. The $n \geq 14$ catalogue has $N_g = 36527$, with a galaxy cluster sky density of 0.34deg^{-2}. Stevenson et al. (1988) selected clusters similarly to Myers et al. (2003) and found a cluster sky density of 3.96deg^{-2} for $n \geq 7$ and 0.4deg^{-2} for ≥ 14. So our cluster sky densities are in reasonable agreement with the expected sky densities. Fig. 5.1 shows a patch of sky in the SGC from our $n \geq 14$ galaxy group sample. The cross-correlations between the galaxy cluster and quasar catalogues are performed between quasars and individual members of each galaxy cluster rather than the center of the clusters. Therefore, the larger clusters are weighted more heavily.

5.2.3 Galaxy Sample

To perform the cross-correlation analyses of our quasar candidate catalogue and individual galaxies, we also generate galaxy catalogues from the VST ATLAS data. We require that all objects have a morphological classification in the $r-$ bands as an extended source. To provide an accurate comparison to the work done on SDSS data by Scranton et al. (2005), we require the galaxies to have detections to $r_{Kron} < 21$, using a 0.15 mag offset to convert to SDSS magnitudes, ie $r_{sdss} = r_{Kron} - 0.15$. We reduce stellar contamination in the galaxy catalogue by performing a cut in r_{A3} v. $r_{A3} - r_{Kron}$ space, where we can see a clear separation of stellar and extended sources. Our galaxy sample at $r < 21$ consists of 16x10^6 objects, which gives us a sky density of 3851 deg^{-2}.

5.3 CUTE Cross-Correlation Method

Following Limber's equation, we can express the 3-D correlation function (and power spectrum) as 2-D angular correlations. To calculate the angular cross-correlation, we need both the quasar sample and galaxy/galaxy cluster samples as well as catalogues of random data sets with the same input parameters as our observable data. Therefore, we generate catalogues of uniformly distributed random quasar points covering the same area as our quasar survey with 10 times as many sources as the observable data sets. We repeat this process to generate catalogues of uniformly distributed random points which subtend the same areas as our galaxy and galaxy cluster catalogues as well.

We use the publicly available Correlation Utilities and Two-point Estimates (CUTE) code Alonso (2012) to generate the $D_G D_Q$, $D_G R_Q$, $R_G D_Q$, and $R_G R_Q$ outputs which we need to calculate the angular cross-correlation. Here $D_G D_Q$ denotes the number of data-point pairs drawn from the galaxy sample and quasar sample with separation θ. For $D_G R_Q$ the quasar sample is replaced with the sample of randomly distributed quasar points with the same angular selection function as the data. Similarly, for $R_G D_Q$ the galaxy sample is replaced with our random galaxy sample. The $R_G R_Q$ output is the number of data-point pairs drawn from the two random quasar and galaxy samples. The $\frac{n_G}{n_{RG}}$ denotes the ratio of data points in the galaxy sample and the random galaxy sample. We then use these outputs for both the NGC and SGC samples to calculate the combined, pair-weighted, cross-correlation using

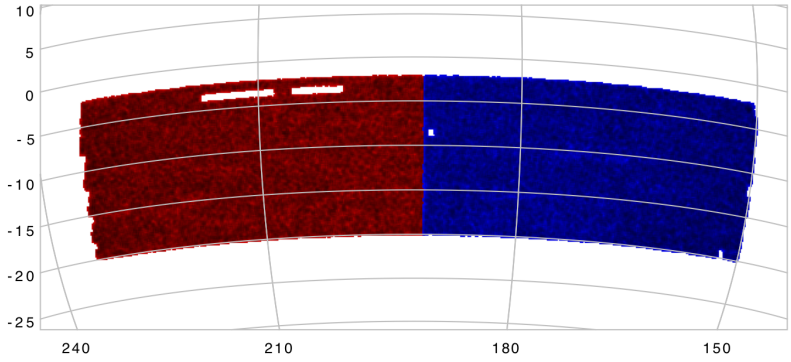

Figure 5.2: Map of our quasar candidates in the NGC, split into 2 equal area regions to calculate error from field-to-field variations. We have masked out areas that are underdense, left as white areas in the map.

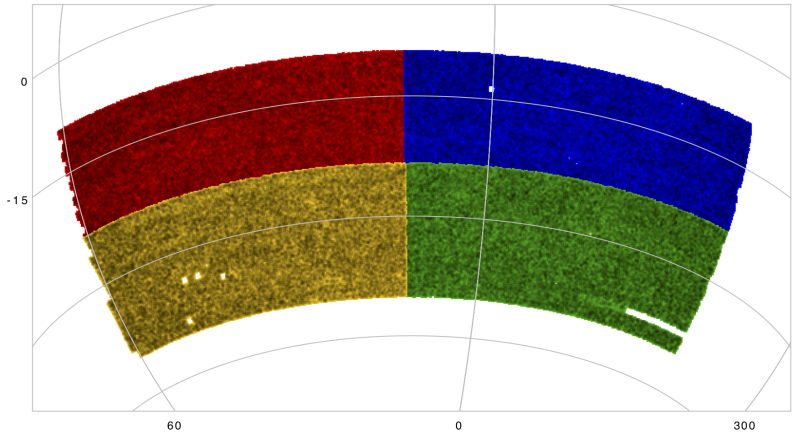

Figure 5.3: Map of our quasar candidates in the SGC, split into 4 equal area regions to calculate error from field-to-field variations. We have masked out areas that are underdense, left as white areas in the map.

a Peebles estimator (Peebles (1980)):

$$\omega_{GQ}(\theta) = \frac{(D_Q D_G)_{NGC} + (D_Q D_G)_{SGC}}{(D_Q R_G) * (\frac{n_G}{n_{RG}})_{NGC} + (D_Q R_G) * (\frac{n_G}{n_{RG}})_{SGC}} - 1, \tag{5.3.1}$$

To take into account error from field-field variations, we divide the quasar and galaxy samples into 6 similarly sized $\sim 670 deg^2$ regions, 2 in the NGC and 4 in the SGC. These fields are shown in Fig. 5.2 and Fig. 5.3. Then we estimate the standard errors of the cross-correlation by using the field-field error:

$$\sigma_{\bar{\omega}(\theta)} = \frac{\sigma_{N_s-1}}{\sqrt{N_s}} = \sqrt{\frac{\sum(\omega_i(\theta) - \bar{\omega_i}(\theta))^2}{N_s^2 - N_s}}, \tag{5.3.2}$$

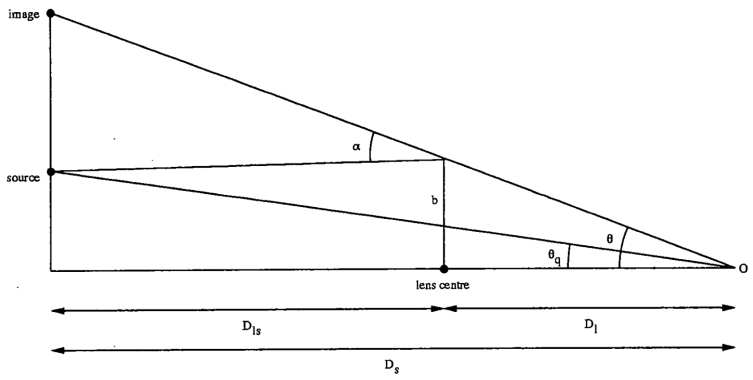

Figure 5.4: Here we show the geometric relations used in Eq. 5.4.1. The figure is taken from Croom (1997).

5.4 Quasar-Galaxy Cluster Cross-Correlation

5.4.1 Quasar-Galaxy Cluster Weak Lensing Model

The lensing of the background objects depends on the mass profiles of the foreground objects. For our work we assume the simplest mass profile of a singular isothermal sphere (SIS). We refer to Myers et al. (2003) to model the lensing caused by a SIS. The deflection angle of sources by foreground lenses is is given initially by Einstein's formula as:

$$\alpha = \frac{4GM(< b)}{bc^2} = \frac{D_s}{D_{ls}}(\theta - \theta_q), \tag{5.4.1}$$

where b is the radius of the lens, $M(< b)$ is the mass contained within the radius of the lens, D_s is the angular diameter distance from the observer to the source, D_{ls} is the angular diameter distance from the source to the lens, θ is the angle from the observer's line of sight to the image, and θ_q is the angle from the observer's line of sight to the source quasar. This relation is shown in Fig. 5.4, as taken from Croom (1997).

We see an increase in apparent brightness/magnitude of the background object as the surface brightness of the object is conserved, but spread across a larger surface area. Therefore the

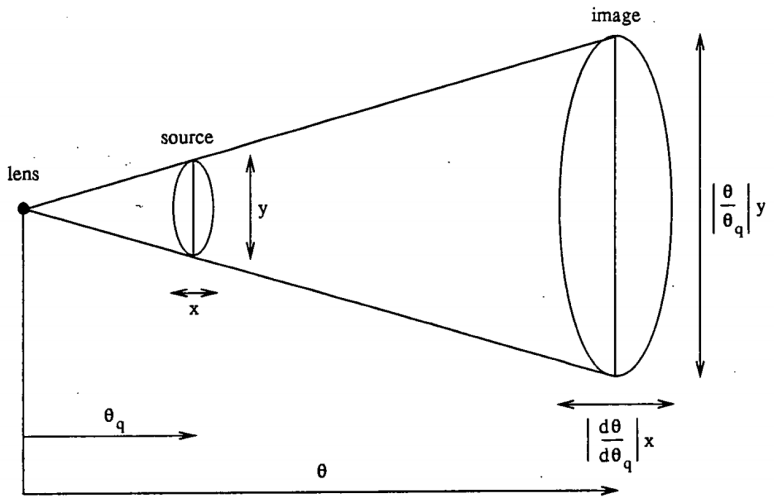

Figure 5.5: Here we show the geometric relations used in Eq. 5.4.2. The figure is taken from Croom (1997).

flux received from the object is increased. This is shown in Fig. 5.5. The magnification, A, of the object due to a foreground lens can be described as:

$$A = |\frac{\theta}{\theta_q}\frac{d\theta}{d\theta_q}| \tag{5.4.2}$$

As we assume lensing by a SIS, we define the mass surface density of a SIS as:

$$\Sigma_{SIS} = \frac{\sigma^2}{2Gr} \tag{5.4.3}$$

where σ is the velocity dispersion of the SIS. This can be integrated over a radius of $r = 0$ to $r = b$ and combined with Eq. 5.4.1 to give the amplification of a background source due to a SIS:

$$A = |\frac{\theta}{\theta - 4\pi(\frac{D_{ls}}{D_s})(\frac{\sigma}{c})^2}| \tag{5.4.4}$$

This amplification factor can also be described as the ratio of the lensed flux and the unlensed flux (Croom (1997)). As the amplification affects the relative distribution of background and

foreground objects, we can relate the angular cross-correlation to the amplification factor through:

$$\omega(\theta) = A^{2.5\alpha-1} - 1 \tag{5.4.5}$$

Where α is the slope of the integrated source number count, $dlog(N)/dm$. Zero correlation is predicted at $\alpha = 0.4$ with an anti-correlation at $\alpha < 0.4$, and a positive correlation at $\alpha > 0.4$.

In our model, we use the flat ΛCDM cosmology, with $\Omega_M = 0.3$ and $\Omega_\Lambda = 0.7$. We assume an average foreground galaxy sample and galaxy cluster redshift of $z = 0.15$ and an average quasar sample redshift of $z = 1.5$. This gives us an angular diameter distance of the quasar sample $D_s = 1780$ Mpc and $D_{ls} = 1235$ Mpc. We also use $\alpha = 0.29$, which is the slope calculated at the faint magnitude end ($g > 20.5$) of the integrated $g-$band quasar number counts in previous works (ie. Myers et al. (2003), Myers et al. (2005)). To find the best-fit value for σ (velocity dispersion), we perform a χ^2 analysis for our $n > 7$ galaxy cluster group as this is the galaxy cluster size which Myers et al. (2003) analyses. We test our model for $800\text{kms}^{-1} < \sigma < 1400\text{kms}^{-1}$ in intervals of 20kms^{-1}. We find a best-fit velocity dispersion of $\sigma = 1200\text{kms}^{-1}$, which we can see by eye in Fig. 5.6. We show this SIS lensing model along with our cross-correlation of the faint $g < 22$ quasar sample and the $n > 7$ galaxy cluster sample in Fig. 5.7. Also shown on this figure is our model with the $\sigma = 1156\text{kms}^{-1}$ value found by Myers et al. (2003).

5.4.2 Faint Quasar - Galaxy Cluster Cross-Correlation Results

We perform this analysis on all of our quasar-galaxy cluster cross-correlations to find the best value for σ for the varying cluster sizes in the cross-correlations. These resulting model with varying values for σ are shown in Fig. 5.8.

The results of the faint quasar-galaxy cluster cross correlation can be seen in Fig. 5.8. We see clear anti-correlation when using the full quasar sample up to depths of $g < 22$. We can roughly check the σ values we find as best-fits in our model using the virial theorem,

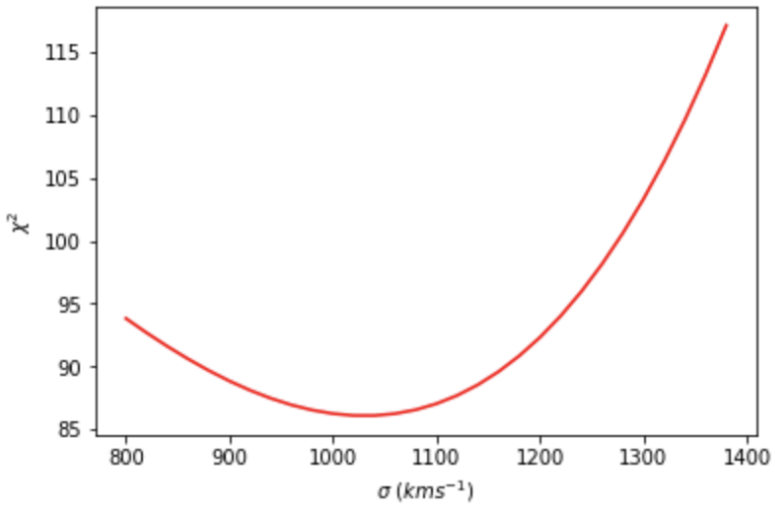

Figure 5.6: Here we show the χ^2 run with σ values in the range of $800 < \sigma < 1400\text{kms}^{-1}$ in intervals of 20.

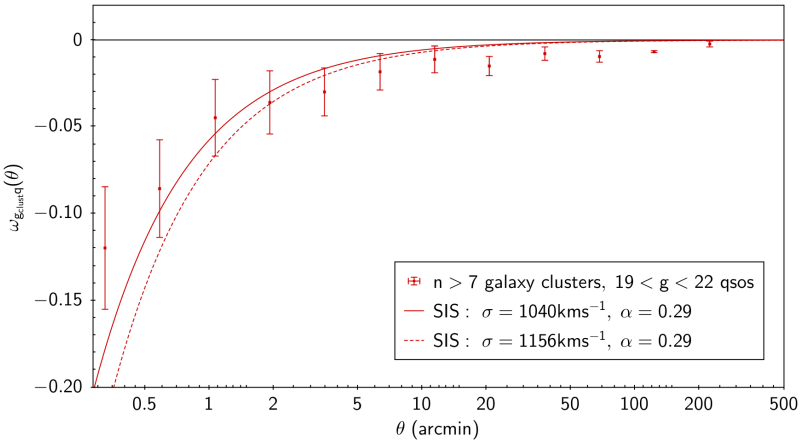

Figure 5.7: We show the cross-correlation of quasars with foreground galaxy clusters of $n > 14$. The model fit we find is shown as a solid line. The model fit with the values used by Myers et al. (2003) is shown as a dashed line.

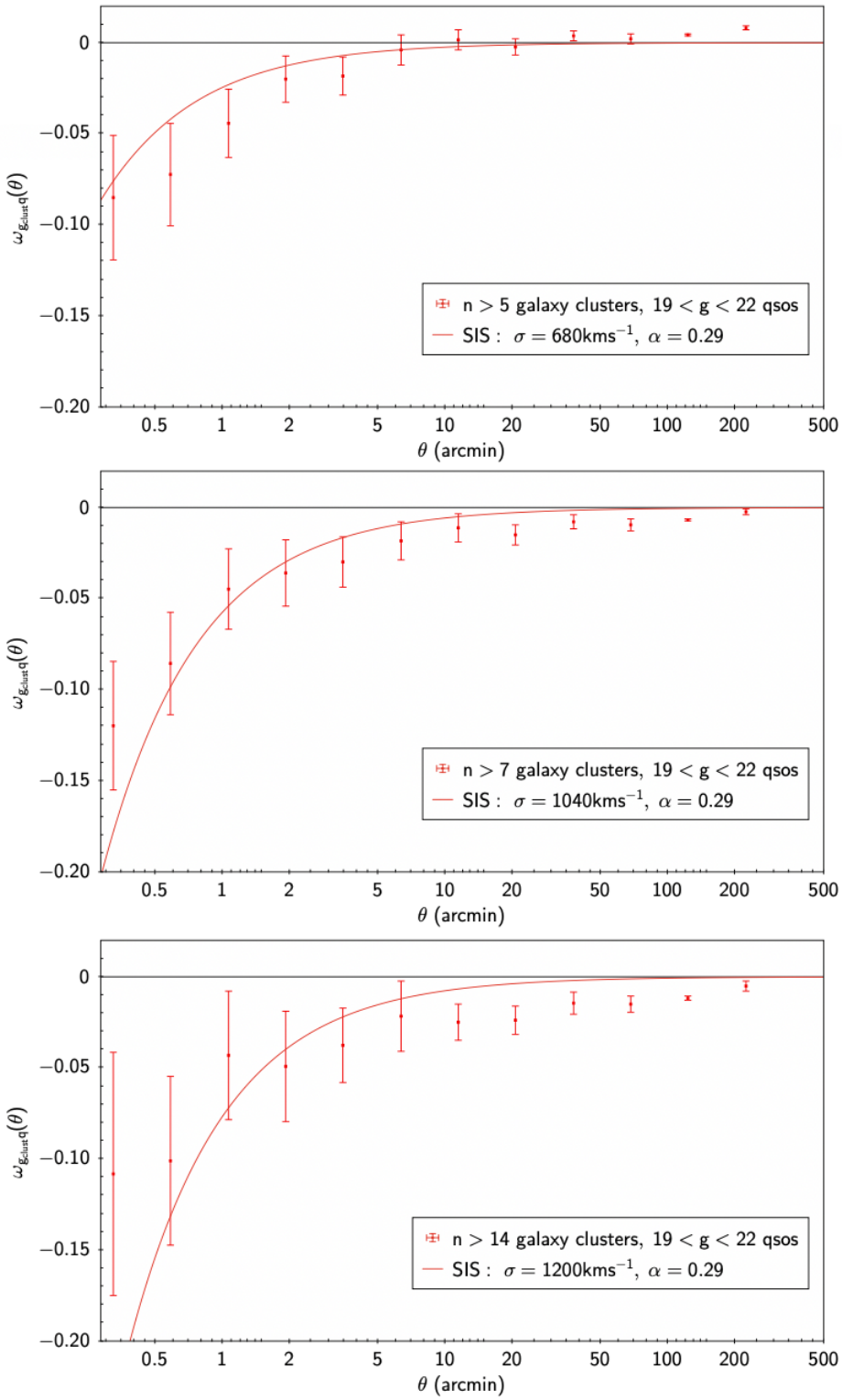

Figure 5.8: Results of the cross-correlation of our quasar candidate catalogue at $g < 22$ and the VST ATLAS southern galaxy cluster catalogue, using the CUTE code for angular cross-correlation. We have included our model fit, as described in Section 5.4.1.

$\sigma^2 \approx \frac{GM}{R}$. From our $19 < g < 22$ run we see that the σ^2 value we get from the $n \geq 14$ clusters is ~ 3 times larger than the σ^2 value we get from the $n \geq 5$ clusters, which is in agreement with the expected results.

5.4.3 Bright Quasar - Galaxy Cluster Cross-Correlation Results

The results of the bright quasar-galaxy cluster cross-correlation are shown in Fig. 5.9. We also see a more positive trending correlation for brighter quasars at $g < 19$, which supports the analysis that our detected anti-correlation is due to lensing, rather than simply due to dust absorption by foreground clusters. For the model used at brighter quasar magnitudes of $17 < g < 19$, we use the α value presented in Scranton et al. (2005) for the $17 < g < 19$ range. We conclude that the bright quasar-cluster cross-correlations are reasonably consistent with the anti-correlation seen at fainter quasar magnitudes, given the hypothesis that both are due to gravitational lensing.

5.5 QSO-Galaxy Sample Cross-Correlation

5.5.1 Quasar-Galaxy Cross-Correlation Model

We use the Williams & Irwin model, as outlined by Myers et al. (2005), to describe the correlation between our quasar sample and foreground galaxies. Although Myers et al. (2005) uses a galaxy sample to $g < 20.5$, we use a galaxy sample of $r < 21$ to be able to compare our results with the SDSS findings by S05. This model compares the auto-correlation of our galaxy sample to the cross-correlation of the quasar and galaxy sample. The lensing convergence κ is defined as:

$$\kappa = \frac{\Sigma(D_l, \theta)}{\Sigma_{cr}(D_l, D_s)}, \tag{5.5.1}$$

where D_l is again the angular diameter distance of the lens, $\Sigma(D_l, \theta)$ is the surface mass density of the lens, and $\Sigma_{cr}(D_l, D_s)$ is the critical mass surface density.

We can estimate the effective convergence using the equation (from Myers et al. (2005)):

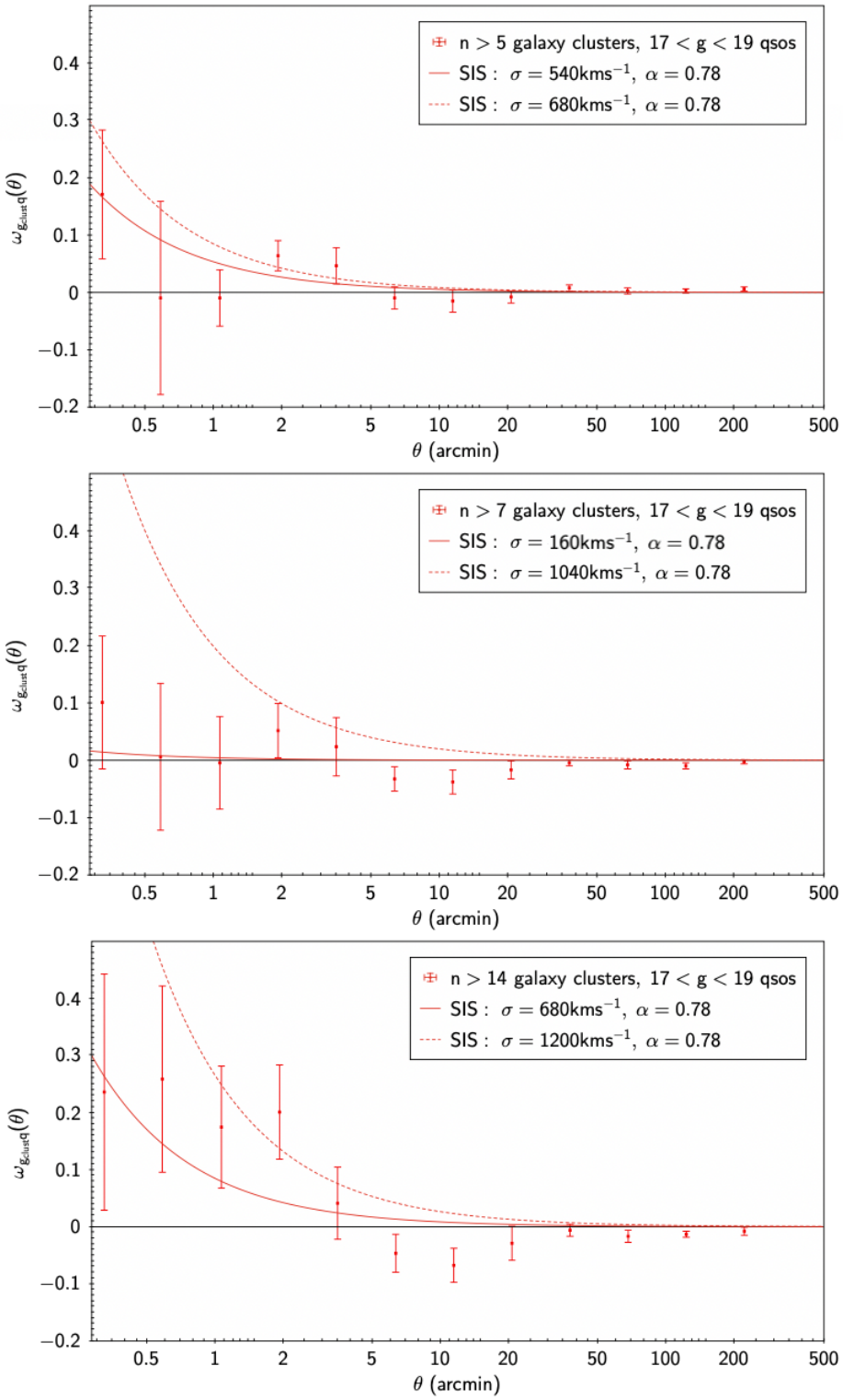

Figure 5.9: Results of the cross-correlation of our quasar candidate catalogue at $g < 19$ and the VST ATLAS southern galaxy cluster catalogue, using the CUTE code for angular cross-correlation. We have included our model fit, as described in Section 5.4.1. As the dispersion velocities seem very low, we also show the model with the dispersion velocities found in the $19 < g < 22$ range.

$$\kappa_{eff}(\theta) = \frac{3H_0^2 c}{8\pi G}(\delta_G - 1)\int_0^{z_{max}} \frac{(1+z)^3 \frac{dt}{dz} dz}{\Sigma_{cr}(z, z_s)}, \tag{5.5.2}$$

As done by Myers et al. (2005), we take $z = 1.5$ as the median redshift of our quasar sample and $z = 0.15$ as the median redshift of our galaxy sample. For our distribution of galaxies, we use $z_{max} = 0.48$ with $\Omega_M = 0.3$, $\Omega_\Lambda = 0.7$. From this calculation, we get a $\bar{\kappa} = 0.025$.

The quasar-galaxy cross-correlation can be estimated using the ω_{gg} and a Taylor expansion of Eq. 5.4.5. Therefore we can model the galaxy-quasar cross-correlation using (Myers et al. (2005)):

$$\omega_{gq}(\theta) = (2.5\alpha - 1)\frac{2\bar{\kappa}}{b}\omega_{gg}(\theta), \tag{5.5.3}$$

where $\frac{\bar{\kappa}}{b} = \frac{\kappa_{eff}(\theta)}{(\delta_G - 1)}$. Here b represents the linear galaxy bias $b = \langle \delta_G - 1 \rangle / \langle \delta_M - 1 \rangle$. The galaxy fluctuation $\langle \delta_G \rangle$ will be estimated via ωgg.

Using our galaxy sample auto-correlation, we fit a power law to the data which gives us $\omega_{gg} = 0.2\theta^{-0.76}$. The value of -0.76 is used in various previous literature for these auto-correlations and we find it also fits well here. We plot our galaxy sample auto-correlation in Fig. 5.10.

5.5.2 Quasar-Galaxy Cross-Correlation Results

Here we present the cross-correlation of our QSO and galaxy catalogues. At angular scales of $\theta < 1$ arcmin, Scranton et al. (2005) (see also Myers et al. (2003), Myers et al. (2005)) notice a clear negative cross-correlation between quasars and foreground galaxies when looking at quasar g-band magnitudes of $g > 20$, as seen in Fig. 5.13. Based on a power law fit estimation, they expect an excess of quasars in the first three magnitude bins and a deficit of quasars at $g > 20$. Here we also detect a clear negative cross-correlation when looking at quasar $g-$band magnitudes of $g > 20$. A more positive trending angular cross-correlation can

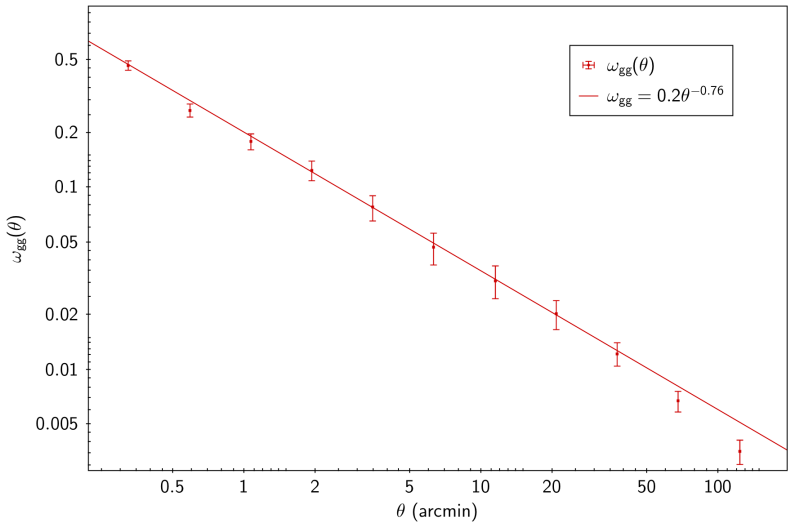

Figure 5.10: The autocorrelation of our galaxy sample at $r < 21$ across the whole sky with our power law fit.

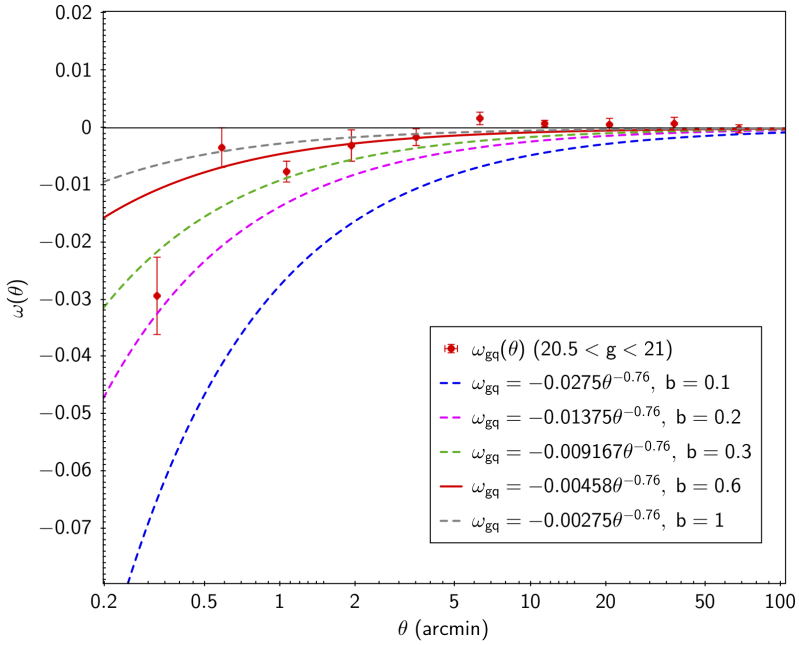

Figure 5.11: Our $\omega_{gg} = 0.2\theta^{-0.76}$ model fit, with $\bar{\kappa} = 0.025$ and $\alpha = 0.29$, with bias values of $b = 0.1$, $b = 0.2$, $b = 0.3$, $b = 0.6$, and $b = 1.0$ for our cross-correlation at $20.5 < g < 21$.

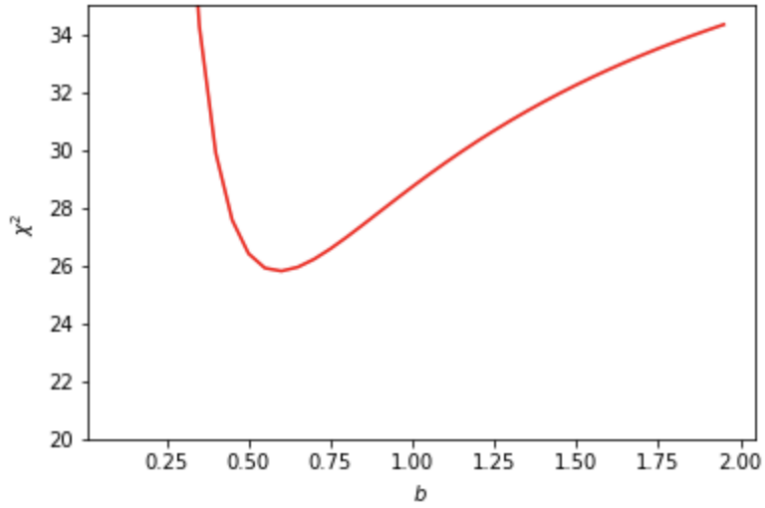

Figure 5.12: χ^2 values for bias in the range of $0.1 < b < 2$ in incremental steps of 0.05, where $b = 0.6$ gives us the minimum χ^2 value.

be seen in the brighter magnitude intervals. We also see a clear negative cross-correlation in the $21 < g < 22$ magnitude range, which probes deeper than Scranton et al. (2005).

Using our $\omega_{gg} = 0.2\theta^{-0.76}$ fit, with $\bar{\kappa} = 0.025$ and $\alpha = 0.29$, we see from Fig. 5.11 that the value of $b =\sim 0.6$ creates the best fit model for our cross-correlation at $20.5 < g < 21$. We also perform a χ^2 test on the model fit for values of b in the range of $0.1 < b < 2$ in incremental steps of 0.05. From that we see that the bias of $b = 0.6$ gives us the minimum $\chi^2(b)$ and is therefore the best fit parameter. This is shown in Fig. 5.12, where we can also see that there is a much steeper slope for smaller values of the bias parameter. Therefore, the error bars on the bias factor are asymetric. For our quasar-galaxy cross-correlation, we detect a bias of $b = 0.6^{+0.18}_{-0.10}$. In these preliminary χ^2 analyses, the covariance between the ω_{gq} points is ignored. Boyle et al. (1988) suggested that these covariances may anyway be sub-dominant.

5.5.3 Quasar-Galaxy Cross-Correlation Comparison With SDSS

To compare to the work done by Scranton et al. (2005) on the lensing detected by the SDSS, we use Eq. 5.5.3 with the values for $\langle \alpha_{S05} - 1 \rangle$ described in Table 1 and Figure 2 of Scranton et al. (2005). We convert these values to fit our model of $(2.5\alpha - 1)$ in the different quasar sample redshift ranges. We first show the Figure 2 from Scranton et al. (2005) to provide a comparison between our two models and data fits in Fig. 5.13.

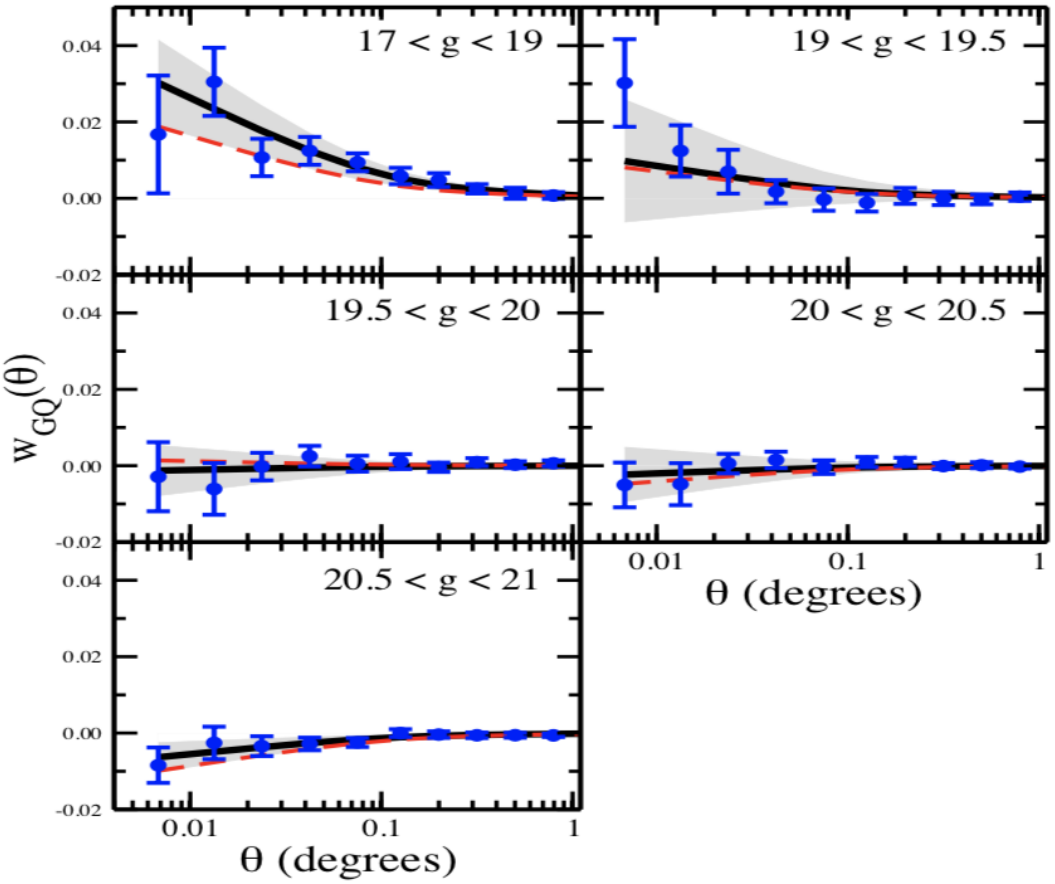

Figure 5.13: The cross-correlation of SDSS quasar candidate catalogue presented in Scranton et al. (2005) at $17 < g < 19$, $19 < g < 19.5$, $19.5 < z < 20$, and $20.5 < g < 21$ and their galaxy catalogue at $r < 21$, using the CUTE code for angular cross-correlation across the full sky.

We show our cross-correlations in Fig. 5.14. In the figures we also show our model fit in red, consistently using a bias value of $b = 0.6$ throughout, as found in Section 5.5.1, and the value for α found by Scranton et al. (2005) for each magnitude bin. The fitting model to the Scranton et al. (2005) data is shown in blue (this corresponds to the dark solid line in Fig. 5.13). From this we see fairly good agreement between our data and the ω_{gq} fitted from the quasar $g-$band number counts from Scranton et al. (2005), however we detect a stronger anti-correlation signal at faint magnitudes.

We also show in Fig. 5.15 a comparison between our model and the model used in Scranton et al. (2005) (denoted by the red dashed line in Fig. 5.13). To compare our models, we assume a bias of $b = 1.0$ instead of $b = 0.6$, as that is roughly consistent with the ΛCDM cosmology, therefore the best comparison with the more sophisticated ΛCDM HOD model assumed by

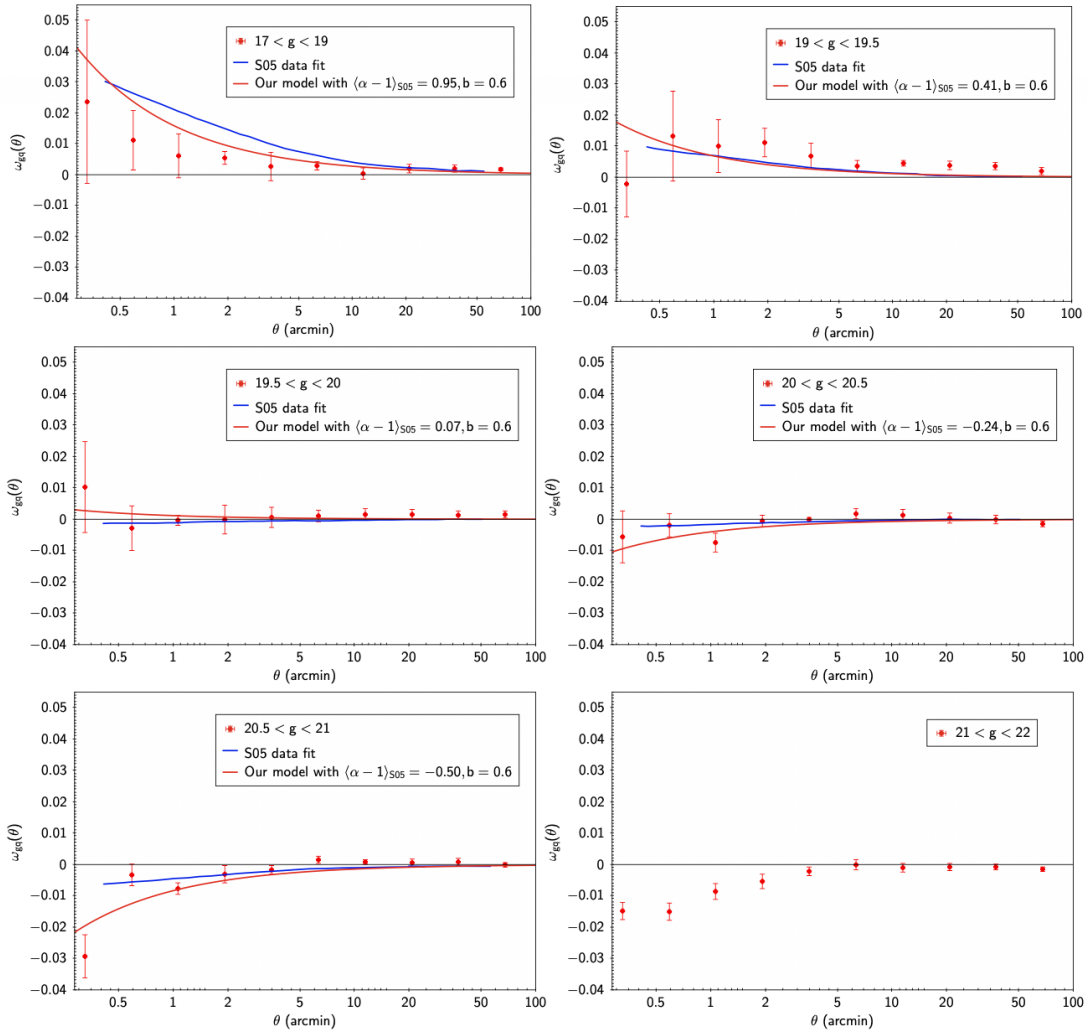

Figure 5.14: Result of the cross-correlation of our quasar candidate catalogue at $17 < g < 19$, $19 < g < 19.5$, $19.5 < z < 20$, $20.5 < g < 21$, and $21 < g < 22$ and our VST ATLAS galaxy catalogue at $r < 21$, using the CUTE code for angular cross-correlation accross the full sky. We also add the Scranton et al. (2005) data fit as well as our model with the and $\langle \alpha - 1 \rangle$ values for each of the quasar $g-$band magnitude bins. A bias value of $b = 0.6$ is consistently assumed. We see that our data is very similar.

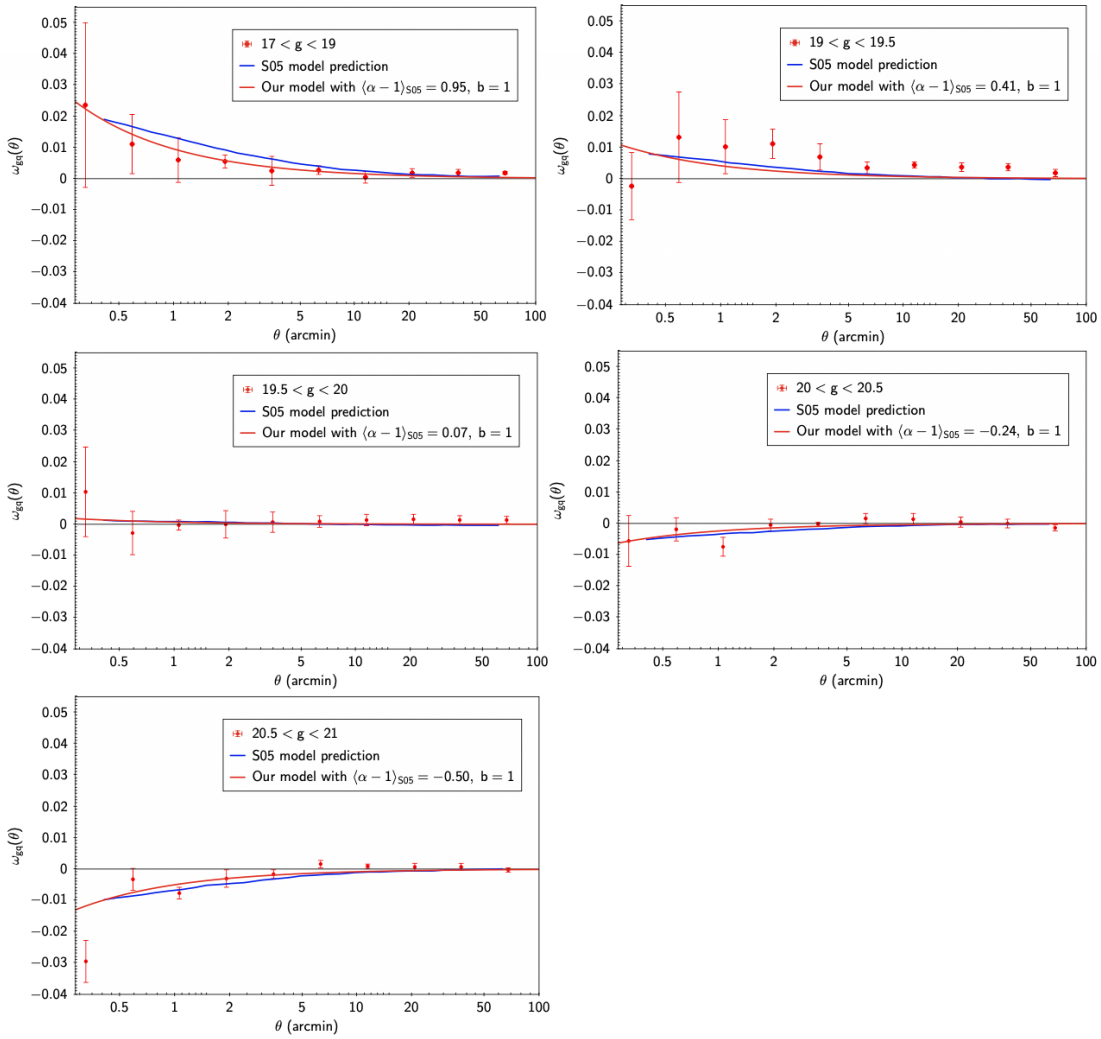

Figure 5.15: Result of the cross-correlation of our quasar candidate catalogue at $17 < g < 19$, $19 < g < 19.5$, $19.5 < z < 20$, $20.5 < g < 21$, and $21 < g < 22$ and our VST ATLAS galaxy catalogue at $r < 21$, using the CUTE code for angular cross-correlation accross the full sky. We also add the Scranton et al. (2005) model fit and $\langle \alpha - 1 \rangle$ values for each of the quasar $g-$band magnitude bins. A bias value of $b = 1.0$ is consistently assumed as this is the bias value assumed in the Scranton et al. (2005) model. Here we can compare our two models.

Scranton et al. (2005). We find relatively good agreement between our two models although We see that their model predicts slightly more lensing than ours with an $\sim 20\%$ offset at the largest deviances. As we see in Fig. 5.12, there is a very shallow slope at $b > 0.6$. Therefore a model with a bias value of $b = 1$ could also be fitted to our data, but since we found $b = 0.6^{+0.18}_{-0.1}$ then $b = 1.0$ is rejected at the 2.2σ level by our data.

As we assume some contamination in our quasar sample, we can also assume that the bias factor is offset by this contamination percentage. In our full quasar catalogue, we assume an efficiency of $\sim 60\%$. This contamination means that our bias factor would be reduced from $b = 0.6$ to $b =\sim 0.4$. As we are using a restricted version of our quasar sample to reduce contamination for the cross-correlation, the actual bias is more likely to be between $0.4 < b < 0.6$. This would mean our rejection of the $b = 1$ model was in the range $2.2 - 3.3\sigma$.

We conclude that our model prediction for QSO-galaxy lensing broadly agrees with that of Scranton et al. (2005) but we observe more anti-correlation. This discrepancy is in the same direction as Myers et al. (2003) although they found a more extreme result with $b \sim 0.1$ using the WI model.

Chapter 6

QSO - Planck CMB Lensing

6.1 Introduction

As the CMB provides a background to all of the observable structures in the universe, we can use the deflection of CMB photons to trace large scale structure and the matter density field. Quasars are great tracers of large scale structure as well as the distribution of dark matter as they are visible across a wide redshift range. As they are biased tracers of the mass distribution in the universe, we calculate this quasar bias to put them in cosmological context and to evaluate the relationship between this bias and the host dark matter halo mass. Here we follow recent works of Han et al. (2019) and particularly Geach et al. (2019), who argue that the cross-correlation of the CMB lensing convergence map and a quasar sample offers a more precise way of measuring the quasar bias than the more commonly used two-point auto-correlation function (e.g. Chehade et al. (2016)) for quasar samples as they are less likely to be affected by systematics such as the quasar and/or galaxy samples. Measuring the deflection of CMB photons also allows us to utilize weak lensing at higher redshifts than possible with quasar-galaxy cross-correlation.

Another CMB lensing study has been done by Krolewski et al. (2019) using unWISE extended sources in three different redshift bins, which have been selected using photometric cuts as well as a non-point-like morphological classification in Gaia. Their samples are then cross-correlated with the most recent release of the Planck CMB lensing maps as well. Although these authors used quasars to calibrate redshifts for galaxy samples selected by unWISE, they did not measure CMB lensing due to quasars.

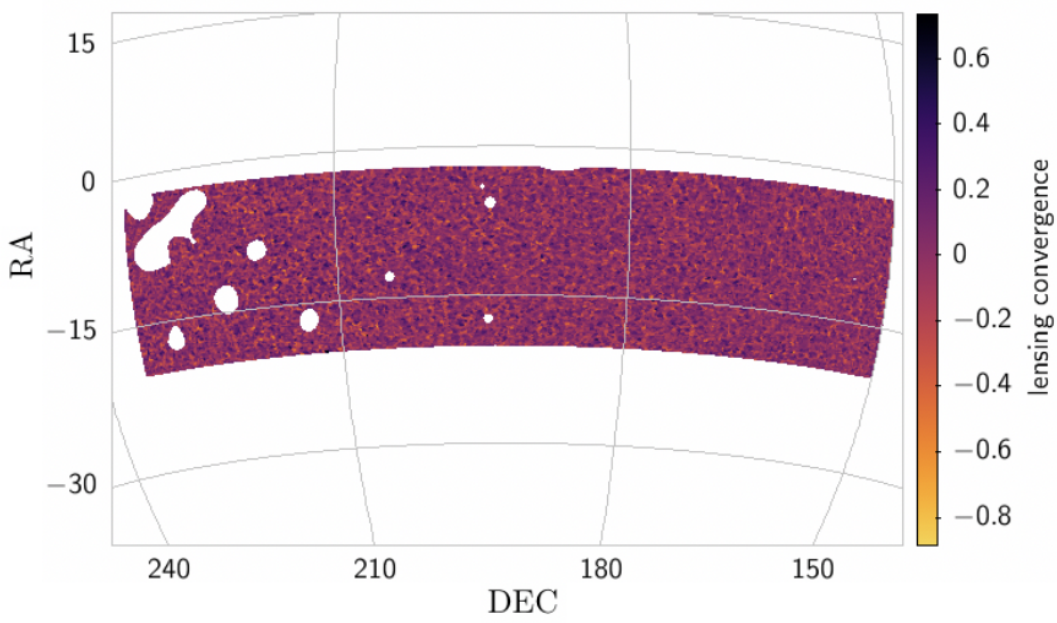

Figure 6.1: The CMB lensing map in the NGC. The masked areas are left in white.

6.2 CMB Lensing Cross-Correlation Data Catalogues

To perform our cross-correlation, we use the 2018 release of the Planck lensing convergence baseline map, using the CMB-only minimum variance estimates of the lensing signal to scales of $l = 4096$ (Planck Collaboration et al. (2018)). Small angular scales correspond to a high l value as $\theta \sim \frac{180^\circ}{l}$. The Healpix a_{lm} are first smoothed with a Gaussian filter with a FWHM of 15 arcmin. We then convert this baseline Minimum Variance lensing map from the stored convergence spherical harmonics a_{lm} to a Healpix map (as done by Geach et al. (2019)) with nside= 2048 and an $l_{max} = 4096$. This then gives us an RA DEC file with coordinates of the healpix pixel centers. We apply the lensing mask provided by the Planck Collaboration et al. (2018) to the CMB data and select two areas that overlap our $\sim 4000\text{deg}^2$ QSO sample, as described in Chapter 4 and shown in Fig. 4.4 and Fig. 4.5. The lensing maps we use in our work are shown in Fig. 6.1 and Fig. 6.2.

In their analysis, Geach et al. (2019) select a sample of 197784 quasars from the SDSS DR14 quasar catalog in the $0.9 \leq z \leq 2.2$ redshift range with a luminosity cut of $M_i(z = 2) \leq -24$, having removed radio-loud quasars from the original catalogue as well. They also utilize the 2018 release of the Planck lensing convergence baseline map.

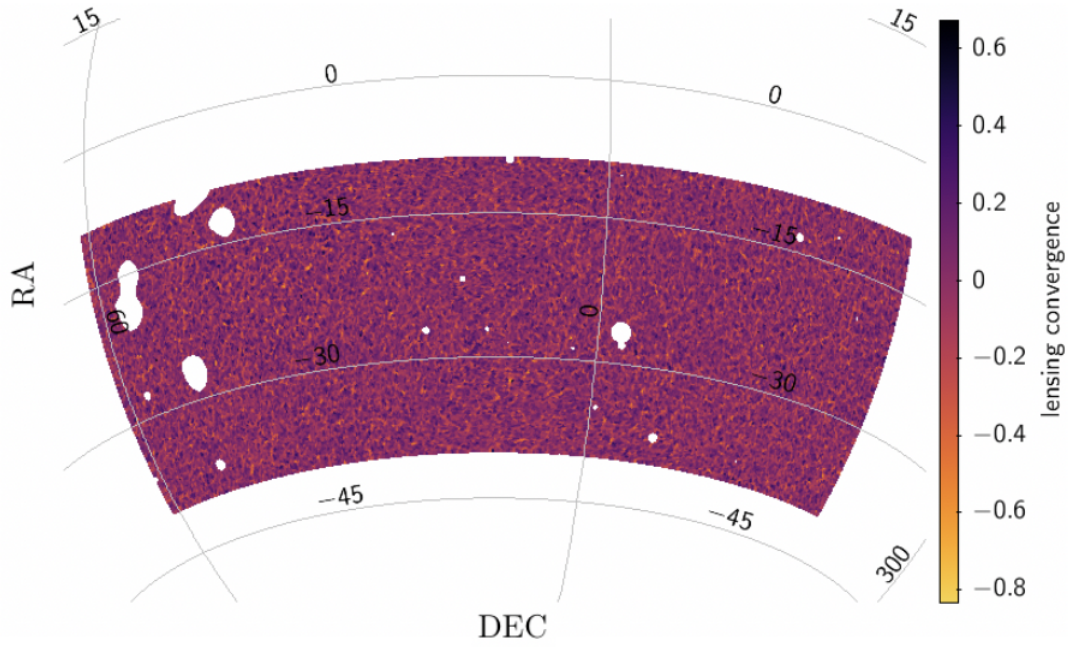

Figure 6.2: The CMB lensing map in the SGC. The masked areas are left in white.

6.3 QSO-CMB Lensing Cross-Correlation

6.3.1 Quasar-CMB Lensing Cross-Correlation Model

As we are using the same CMB lensing data catalogue and similar quasar samples as Geach et al. (2019), we perform our analysis using the model described in their work. The model includes a lensing convergence contribution made by a 1−halo and a 2−halo term. Similarly to the equation used in the previous chapter, Eq. 5.5.1, the convergence due to the 1-halo term is defined as:

$$\kappa_1(R) = \frac{\Sigma(R)}{\Sigma_{crit}} \tag{6.3.1}$$

where $\Sigma(R)$ is the projected mass surface density given an NFW density profile, and Σ_{crit} is the critical surface density. Here the projected mass surface density is:

$$\Sigma(R) = 2\int_R^{\text{inf}} \frac{r\rho r}{\sqrt{(r^2 - R^2)}} dr \tag{6.3.2}$$

The 2−halo term is described by:

$$\kappa_2(\theta) = \frac{\bar{\rho}(z)}{(1+z)^3 \Sigma_{crit} D^2(z)} \int \frac{ldl}{2\pi} J_0(l\theta) b_h \triangle(k,z) \tag{6.3.3}$$

where J_0 is a Bessel function of the zeroth order, $D(z)$ is the angular diameter distance (shown as $D(s)$ in Fig. 5.5), $\triangle(k,z)$ is the linear matter power spectrum, $\bar{\rho}(z)$ is the average density of the Universe at z and b_h is the quasar bias for a halo of mass M_h. Then, the final model for the lensing convergence is:

$$< \kappa >= \int dz(\kappa_1 + \kappa_2) dn/dz \tag{6.3.4}$$

We show in Fig. 6.3 the lensing convergence results obtained by Geach et al. (2019) through their quasar stacking method, taken from their Figure 3. They show the radial profile of the quasar stacked convergence along with the best fitting lensing model as a solid line. The model includes the 1- and 2-halo contribution to the lensing signal, although at scales of $\theta > 15'$, the 1−halo term is mostly filtered out. Below, we shall be simply scaling the Geach et al model in b_h and hence effectively ignoring the 1−halo term.

In our analysis we assume that we have the same absolute magnitude range as Chehade et al. (2016). We also use a comparable quasar sample to Geach et al. (2019). However, our photometric redshifts are less accurate and therefore it may not be worth splitting up in to redshift and/or magnitude bins to perform further analysis.

6.3.2 Quasar-CMB Lensing Cross-Correlation Results

The CMB lensing convergence denoted by κ is a projection of a 3D density field. The quasar density is also a projection of a 3D density field. We convert these 3D projections into angular comoving distances in order to perform angular correlations.

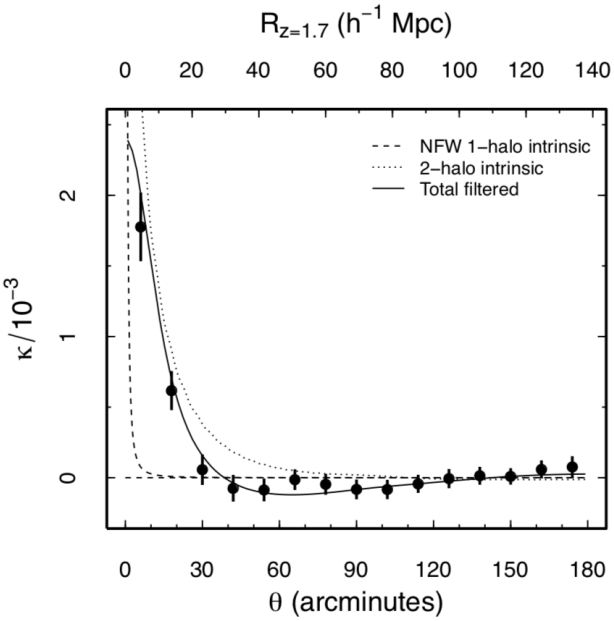

Figure 6.3: Here we show the results from the Geach et al. (2019) cross-correlation between foreground quasars and the CMB lensing map. The model is described in Section 6.3.1.

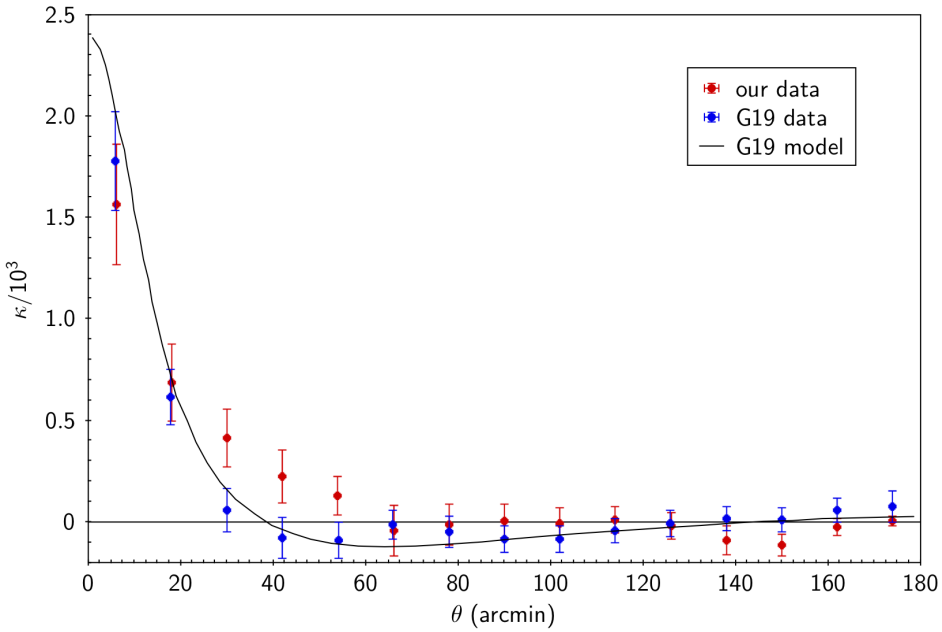

Figure 6.4: We show our VST ATLAS+unWISE QSO-CMB Lensing cross-correlation result along with the result and model obtained by Geach et al. (2019) (denoted by the dark solid line in Fig. 6.3).

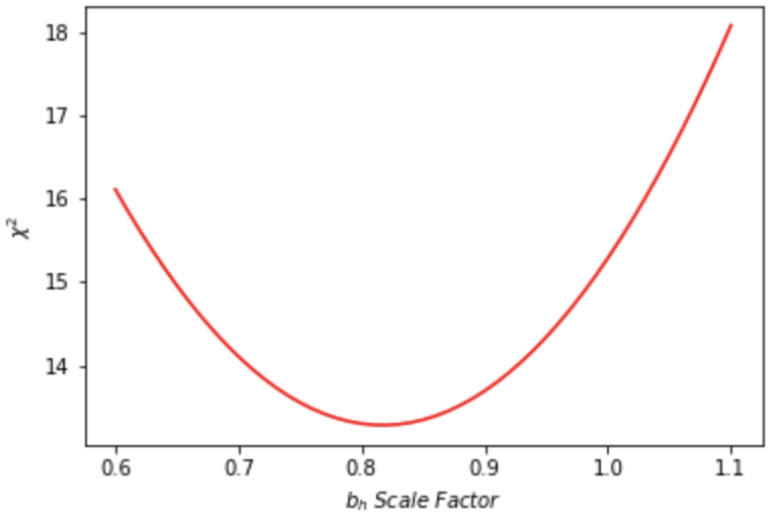

Figure 6.5: χ^2 values for different bias values, where a scale factor of 0.82 gives us the minimum χ^2 value.

Results of the cross-correlation we perform between our quasar sample and the Planck CMB Lensing map can be seen in Fig. 6.4. We show our results along with the model fit found by Geach et al. (2019), denoted by the solid dark line in Fig. 6.3. We note that the errors on our results are reasonably comparable to those of Geach et al. (2019). The main difference between the two results is between 30-60 arcmin where our results are slightly higher.

We can see from Eq. 6.3.3 that the 2−halo lensing convergence term scales with b_h. Therefore, we can infer our b_h by fitting a scaled version of the model found in Geach et al. (2019) to our data. We look at the $0' < \theta < 60'$ range as our data falls below $\kappa = 0$ at larger scales. The Geach et al. (2019) model also falls below $\kappa = 0$ at scales of $\theta > 40'$. The negative cross-correlations predicted at large scales by this model may arise as we smoothed the spherical harmonics (the a_{lm}) before converting this to a Healpix map with the healpy alm2map routine. Additionally, there are most likely more systematics at larger scales, despite the errors being smaller. Therefore, we only fit the $0 - 60$ arcminute range where we find a best-fit scaling factor of 0.82. We also find that the model presented in Geach et al. (2019) is consistent with our result at the 1.4σ level. The χ^2 fit is shown in Fig. 6.5. However, we note that this χ^2 fit and associated errors are only approximate as they do not take into account covariance between data points. After having found the 0.82 scale factor offset between our data and the Geach et al. (2019) model, we show our data along with the scaled version of the model fit found in Geach et al. (2019) in fig. 6.6.

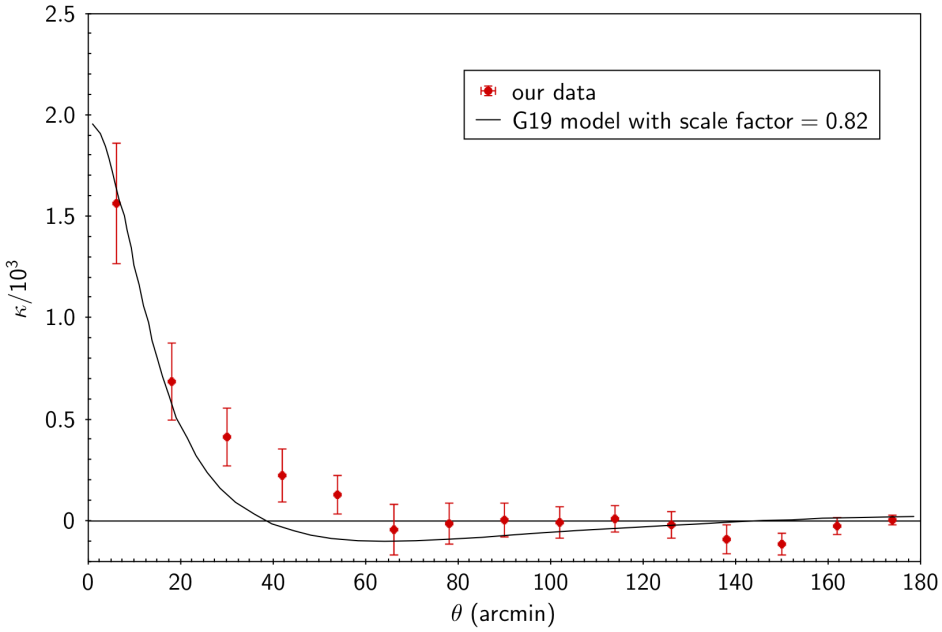

Figure 6.6: We show our VST ATLAS+unWISE QSO-CMB Lensing cross-correlation result along with the model obtained by Geach et al. (2019) multiplied by the scale factor of 0.82 which we found with a χ^2 test.

After finding the scale factor, we can determine our b_h by scaling the b_h found in Geach et al. (2019). They state that their measured quasar halo bias is $b_h = 2.7 \pm 0.3$ at $z = 1.7$ for quasars with $M_i < -24$ mag. Therefore, we measure a quasar halo bias of $b_h = 2.2 \pm 0.12$ at $z = 1.7$.

In Figure 14 of Chehade et al. (2016), they show the bias they determined as a function of redshift and absolute magnitude. We plot in Fig. 6.7, Figure 14 as it is presented in Chehade et al. (2016) along with our bias measurement of $b_h = 2.2 \pm 0.12$, shown as a red point. The bias result of of $b_h = 2.7 \pm 0.3$ at $z = 1.7$ found by Geach et al. (2019) is shown as a blue point. The dotted black line represents the bias result determined by Chehade et al. (2016) and the bias result from 2QZ is shown as a dashed black line. Also in the figure is the measurement of the quasar halo bias from the BOSS survey determined by Chehade et al. (2016). The solid grey line represents the evolution for a halo of mass $2 \times 10^{12} h^{-1} \mathrm{M}_{\odot}$. From this figure, we see that the quasar halo bias measured by Geach et al. (2019) is in line with the bias measured 2QZ, but falls above the bias found by Chehade et al. (2016) (the black dotted line). Our measurement of the quasar halo bias falls in line with the bias found by Chehade et al. (2016). Overall there seems to be good agreement between the quasar-CMB lensing results of Geach et al. (2019) and ourselves. There also seems to be excellent agreement of these results with those derived from quasar clustering.

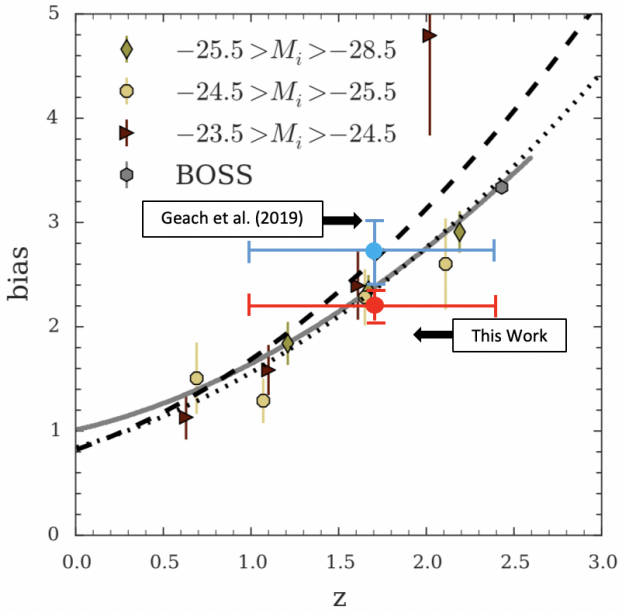

Figure 6.7: The quasar halo bias as a function of redshift, taken from Figure 14 of Chehade et al. (2016). We show the b_h value found by Geach et al. (2019) in blue and our b_h in red.

Chapter 7

Summary and Conclusions

The aim of this thesis was to generate the VST-ATLAS quasar catalogue and perform initial gravitational lensing science. We did this by looking at photometric quasar selection work done in Chehade et al. (2016), and then using additional William Herschel Deep Field and DESI analyses to optimize selections. With a conservative version of this quasar catalogue, we are able to perform weak gravitational lensing analyses through the cross-correlation of our quasar sample and foreground galaxies and galaxy clusters. We also perform a cross-correlation of the quasar sample with the Planck CMB lensing maps.

Having described the various imaging and spectroscopic surveys we use in Chapter 2, in Chapter 3 we present the methods for our quasar candidate selection. Our aim was to generate a catalogue with a quasar sky density of 130deg^{-2} in order to have a quasar selection that is comparable to the expected quasar catalogues outlined in DESI Collaboration et al. (2016). To achieve this aim, we utilize initial VST-ATLAS photometric selection methods outlined in Chehade et al. (2016). We then perform an analysis of the spectroscopically confirmed quasars in the WHDF to see how X-ray selected quasars can inform our photometric selections. An analysis and comparison done with the photometric selections outlined in DESI Collaboration et al. (2016) further informs our selections to obtain our final quasar catalogue. Through these analyses we determine that the inclusion of objects that have been mis-identified as galaxies, and exhibit quasar colors in $ugriW1$, gives us the most complete catalogue of quasar candidates. The resulting quasar sky density over our full $\sim 4000\text{deg}^2$ is 204deg^{-2}, with ~ 704000 stellar quasar candidates and a total of ~ 850000 combined stellar and mis-identified extended source candidates. We find $\sim$ 85% completeness and $\sim$ 60% efficiency, therefore we determine a final quasar sky density of $\sim 120\text{deg}^{-2}$.

In Chapter 4 we have presented the full VST ATLAS Quasar Survey. We also perform a $g-$band number count comparison with the work done in Palanque-Delabrouille et al. (2016). We use their models as these are used by DESI to determine their expected quasar number counts. Therefore, we are able to see how our photometric selection methods compare to the selection method based on the quasar luminosity function. We find almost perfect agreement between our expected number counts of 204deg^{-2} at $g < 22.5$ and the number counts predicted by the quasar luminosity function PLE+LEDE model, which predict a quasar sky density of 195deg^{-2}. However, we must take into account our expected stellar contamination. Additionally, the QLF model predicts sky densities for larger redshift ranges than we are probing. Therefore, we determine that the expected quasar sky density for the comparable $0.8 < z < 2.2$ redshift range expected from the QLF PLE+LEDE model is 141deg^{-2}. In this chapter we also use the ANNz2 algorithm to obtain initial photometric redshifts for our quasar sample. Through this we determine an average redshift of our quasar sample of $z \sim 1.7$, with a spike at $z = 1.8$. Inconsistencies in our training samples in the NGC and SGC may account for the features and irregularities we notice in the redshift distribution of our quasar sample.

In Chapter 5 we perform a cross-correlation of a conservative version of our VST ATLAS+unWISE quasar catalogue, described in Chapter 4 with foreground galaxy clusters (Ansarinejad et al. (2019, in prep)). We see a clear anti-correlation at faint quasar magnitudes ($19 < g < 22$), and a positive trending correlation at bright quasar magnitudes ($17 < g < 19$). Using the method outlined in Myers et al. (2003), we derive a model for the lensing of background quasars by foreground galaxy clusters, which we define as a Singular Isothermal Sphere (SIS). We confirm the Myers et al. (2003) result and then use it as a first order test of our data to determine that our quasar sample has reasonably low stellar contamination. Through the cross-correlation of faint quasars ($19 < g < 22$) and galaxy clusters with $n \geq 7$, we determine the velocity dispersion of $n \geq 5$, $n \geq 7$, and $n \geq 14$ clusters. These σ results are roughly checked using the virial theorem to find that our σ^2 measurement for $n \geq 14$ clusters is ~ 3 times larger than the σ^2 measurement for $n \geq 5$ clusters, which is in general agreement with the expected value.

Also shown in Chapter 5 is the cross-correlation of our conservative VST ATLAS+unWISE quasar catalogue with foreground VST-ATLAS galaxies. We find a negative correlation at

quasar magnitudes of $g > 20$ and a positive correlation at brighter magnitudes. We confirm our results by comparing to the measured result of Scranton et al. (2005), where we find reasonable agreement between our measurements of the cross-correlation in multiple $g-$band magnitude bins. Using a Williams & Irwin model for galaxy-quasar lensing, we find a quasar bias of $b = 0.6^{+0.18}_{-0.10}$, and therefore reject the $b = 1$ value assumed by the ΛCDM model at the 2.2σ level. We conclude that our model prediction for QSO-galaxy lensing broadly agrees with that of Scranton et al. (2005) but we observe more anti-correlation. This discrepancy is in the same direction as Myers et al. (2003) although they found a more extreme result with $b \sim 0.1$ using the Williams & Irwin model.

In Chapter 6 we cross-correlate our VST-ATLAS+unWISE quasar catalogue with the CMB lensing maps published by Planck Collaboration et al. (2018). We utilize methods outlined by Geach et al. (2019) to detect lensing of the CMB by foreground quasars. Here we find good agreement between our data and the Geach et al. (2019) data, and are able to fit their model to our data with a scaling factor of 0.82. Therefore, we are able to measure a quasar halo bias of $b_h = 2.0 \pm 0.12$ at an average redshift of $z = 1.7$. Finally, we determine that our bias value is in excellent agreement with the quasar bias from quasar clustering in Chehade et al. (2016).

This work was intended to show preliminary results using photometric data. More exact work will be done with the spectroscopic data from the completed eROSITA AGN and 4MOST Cosmology Redshift Surveys. This will include the long-term aims of the VST ATLAS Quasar Survey, as mentioned in Chapter 1, which is to perform BAO and redshift space distortion analyses to probe the nature of dark energy and dark matter.

Bibliography

Alonso, D. *CUTE solutions for two-point correlation functions from large cosmological datasets.* arXiv e-prints (2012), arXiv:1210.1833. 1210.1833.

Ansarinejad, B., Murphy, D., Shanks, T., et al. *The VST ATLAS Southern Galaxy Catalogue* (2019, in prep).

Bielby, R.M., Hill, M.D., Metcalfe, N., et al. *Submillimetre observations of X-ray active galactic nuclei in the William Herschel Deep Field.* MNRAS, **419**(2) (2012), 1315. 1108.3934.

Boyle, B.J., Croom, S.M., Shanks, T., et al. *The 2dF QSO Redshift Survey.* In N. Metcalfe, T. Shanks, editors, *A New Era in Cosmology*, volume 283 of *Astronomical Society of the Pacific Conference Series* (2002), page 72.

Boyle, B.J., Fong, R., Shanks, T. *On the correlation of UVX QSOs with galaxies.* MNRAS, **231** (1988), 897.

Chehade, B., Shanks, T., Findlay, J., et al. *The 2QDES Pilot: the luminosity and redshift dependence of quasar clustering.* MNRAS, **459**(2) (2016), 1179. 1603.04849.

Colless, M., Dalton, G., Maddox, S., et al. *The 2dF Galaxy Redshift Survey: spectra and redshifts.* MNRAS, **328**(4) (2001), 1039. astro-ph/0106498.

Croom, S.M. Ph.D. thesis, - (1997).

Croom, S.M., Boyle, B.J., Shanks, T., et al. *The 2dF QSO Redshift Survey - XIV. Structure and evolution from the two-point correlation function.* MNRAS, **356**(2) (2005), 415. astro-ph/0409314.

da Ângela, J., Shanks, T., Croom, S.M., et al. *The 2dF-SDSS LRG and QSO survey: QSO clustering and the L-z degeneracy.* MNRAS, **383**(2) (2008), 565. astro-ph/0612401.

DESI Collaboration, Aghamousa, A., Aguilar, J., et al. *The DESI Experiment Part I: Science,Targeting, and Survey Design.* arXiv e-prints (2016), arXiv:1611.00036. 1611.00036.

Eisenstein, D.J., Zehavi, I., Hogg, D.W., et al. *Detection of the Baryon Acoustic Peak in the Large-Scale Correlation Function of SDSS Luminous Red Galaxies.* ApJ, **633**(2) (2005), 560. astro-ph/0501171.

Geach, J.E., Peacock, J.A., Myers, A.D., et al. *The Halo Mass of Optically Luminous Quasars at $z \approx$ 1-2 Measured via Gravitational Deflection of the Cosmic Microwave Background.* ApJ, **874**(1) (2019), 85. 1902.06955.

González-Solares, E.A., Walton, N.A., Greimel, R., et al. *Initial data release from the INT Photometric Hα Survey of the Northern Galactic Plane (IPHAS).* MNRAS, **388** (2008), 89. 0712.0384.

Han, J., Ferraro, S., Giusarma, E., et al. *Probing gravitational lensing of the CMB with SDSS-IV quasars.* MNRAS, **485**(2) (2019), 1720. 1809.04196.

Kaiser, N. *Clustering in real space and in redshift space.* MNRAS, **227** (1987), 1.

Kaiser, N. *Weak Lensing and Cosmology.* ApJ, **498**(1) (1998), 26. astro-ph/9610120.

Kaiser, N., Squires, G. *Mapping the dark matter with weak gravitational lensing.* ApJ, **404** (1993), 441.

Krolewski, A., Ferraro, S., Schlafly, E.F., et al. *unWISE tomography of Planck CMB lensing.* arXiv e-prints (2019), arXiv:1909.07412. 1909.07412.

Kuijken, K., Bender, R., Cappellaro, E., et al. *OmegaCAM: the 16k×16k CCD camera for the VLT survey telescope.* The Messenger, **110** (2002), 15.

Merloni, A., Predehl, P., Becker, W., et al. *eROSITA Science Book: Mapping the Structure of the Energetic Universe.* arXiv e-prints (2012), arXiv:1209.3114. 1209.3114.

Metcalfe, N., Shanks, T., Campos, A., et al. *Galaxy number counts - V. Ultradeep counts: the Herschel and Hubble Deep Fields.* MNRAS, **323** (2001), 795. astro-ph/0010153.

Metcalfe, N., Shanks, T., Weilbacher, P.M., et al. *Galaxy number counts - VI. An H-band survey of the Herschel Deep Field.* MNRAS, **370** (2006), 1257. astro-ph/0509540.

Mo, H.J., White, S.D.M. *An analytic model for the spatial clustering of dark matter haloes.* MNRAS, **282**(2) (1996), 347. astro-ph/9512127.

Mountrichas, G., Shanks, T. *QSO lensing magnification: a comparison of 2QZ and Sloan Digital Sky Survey results.* MNRAS, **380**(1) (2007), 113. astro-ph/0701870.

Murphy, D.N.A., Geach, J.E., Bower, R.G. *ORCA: The Overdense Red-sequence Cluster Algorithm.* MNRAS, **420**(3) (2012), 1861. 1109.3182.

Myers, A.D., Outram, P.J., Shanks, T., et al. *The 2dF QSO Redshift Survey - X. Lensing of background QSOs by galaxy groups.* MNRAS, **342**(2) (2003), 467. astro-ph/0211624.

Myers, A.D., Outram, P.J., Shanks, T., et al. *On statistical lensing and the anticorrelation between 2dF QSOs and foreground galaxies.* MNRAS, **359**(2) (2005), 741. astro-ph/0502481.

Palanque-Delabrouille, N., Magneville, C., Yèche, C., et al. *The extended Baryon Oscillation Spectroscopic Survey: Variability selection and quasar luminosity function.* A&A, **587** (2016), A41. 1509.05607.

Palanque-Delabrouille, N., Yeche, C., Myers, A.D., et al. *Variability selected high-redshift quasars on SDSS Stripe 82.* A&A, **530** (2011), A122. 1012.2391.

Peebles, P.J.E. *The large-scale structure of the universe* (1980).

Peebles, P.J.E., Yu, J.T. *Primeval Adiabatic Perturbation in an Expanding Universe.* ApJ, **162** (1970), 815.

Perlmutter, S., Aldering, G., Goldhaber, G., et al. *Measurements of Ω and Λ from 42 High-Redshift Supernovae.* ApJ, **517** (1999), 565. astro-ph/9812133.

Perlmutter, S., Gabi, S., Goldhaber, G., et al. *Measurements of the Cosmological Parameters Ω and Λ from the First Seven Supernovae at z >= 0.35.* ApJ, **483**(2) (1997), 565. astro-ph/9608192.

Planck Collaboration, Aghanim, N., Akrami, Y., et al. *Planck 2018 results. VIII. Gravitational lensing.* arXiv e-prints (2018), arXiv:1807.06210. 1807.06210.

Ratra, B., Peebles, P.J.E. *Cosmological consequences of a rolling homogeneous scalar field.* Phys. Rev. D, **37** (1988), 3406. URL https://link.aps.org/doi/10.1103/PhysRevD.37.3406.

Richard, J., Kneib, J.P., Blake, C., et al. *4MOST Consortium Survey 8: Cosmology Redshift Survey (CRS).* The Messenger, **175** (2019), 50. 1903.02474.

Riess, A.G., Filippenko, A.V., Challis, P., et al. *Observational Evidence from Supernovae for an Accelerating Universe and a Cosmological Constant.* AJ, **116** (1998), 1009. astro-ph/9805201.

Rubin, V.C., Thonnard, N., Ford, W. K., J. *Extended rotation curves of high-luminosity spiral galaxies. I. The angle between the rotation axis of the nucleus and the outer disk of NGC 3672.* ApJ, **217** (1977), L1.

Sadeh, I., Abdalla, F.B., Lahav, O. *ANNz2: Photometric Redshift and Probability Distribution Function Estimation using Machine Learning.* PASP, **128**(968) (2016), 104502. 1507.00490.

Sakharov, A.D. *The Initial Stage of an Expanding Universe and the Appearance of a Nonuniform Distribution of Matter.* Soviet Journal of Experimental and Theoretical Physics, **22** (1966), 241.

Schlafly, E.F., Meisner, A.M., Green, G.M. *The unWISE Catalog: Two Billion Infrared Sources from Five Years of WISE Imaging.* ApJS, **240**(2) (2019), 30. 1901.03337.

Scranton, R., Ménard, B., Richards, G.T., et al. *Detection of Cosmic Magnification with the Sloan Digital Sky Survey.* ApJ, **633**(2) (2005), 589. astro-ph/0504510.

Shanks, T., Metcalfe, N., Chehade, B., et al. *The VLT Survey Telescope ATLAS.* MNRAS, **451**(4) (2015), 4238. 1502.05432.

Stevenson, P.R.F., Fong, R., Shanks, T. *Correlation analysis of objectively defined galaxy and cluster catalogues.* MNRAS, **234** (1988), 801.

Timlin, J.D., Ross, N.P., Richards, G.T., et al. *SpIES: The Spitzer IRAC Equatorial Survey.* ApJS, **225**(1) (2016), 1. 1603.08488.

Wright, E.L., Eisenhardt, P.R.M., Mainzer, A.K., et al. *The Wide-field Infrared Survey Explorer (WISE): Mission Description and Initial On-orbit Performance.* AJ, **140** (2010), 1868. 1008.0031.

Yang, Q., Wu, X.B., Fan, X., et al. *Quasar Photometric Redshifts and Candidate Selection: A New Algorithm Based on Optical and Mid-infrared Photometric Data.* AJ, **154**(6) (2017), 269. 1710.09155.

Zwicky, F. *Die Rotverschiebung von extragalaktischen Nebeln.* Helvetica Physica Acta, **6** (1933), 110.